ANALYSIS AND IDENTIFICATION OF VORTICES WITHIN A TURBULENT CHANNEL BOUNDARY LAYER FLOW

A Thesis

by

ADRIAN GASTON MARONI VEIGA

Submitted to the Office of Graduate Studies of
Texas A&M University
in partial fulfillment of the requirements for the degree of

MASTER OF SCIENCE

May 2005

Major Subject: Mechanical Engineering

ANALYSIS AND IDENTIFICATION OF VORTICES WITHIN A TURBULENT CHANNEL BOUNDARY LAYER FLOW

A Thesis

by

ADRIAN GASTON MARONI VEIGA

Submitted to Texas A&M University
in partial fulfillment of the requirements
for the degree of

MASTER OF SCIENCE

Approved as to style and content by:

Yassin A. Hassan (Co-Chair of Committee)	Kalyan Annamalai (Co-Chair of Committee)
William H. Marlow (Member)	Dennis O'Neal (Head of Department)

May 2005

Major Subject: Mechanical Engineering

ABSTRACT

Analysis and Identification of Vortices Within a Turbulent Channel Boundary Layer Flow. (May 2005)

Adrian Gaston Maroni Veiga, B.S., Instituto Universitario Aeronautico, Argentina

Co-Chairs of Advisory Committee: Dr. Yassin A. Hassan
Dr. Kalyan Annamalai

Vortical structures are regarded as the dominant organized patterns in wall turbulence. They play a key role in physical phenomena of practical importance such as energy and momentum transport, combustion, mixing, and noise and drag production. Considerable investigations have been performed in drag and noise phenomena studies, with a main purpose of controlling and reducing them. Various techniques to control the drag reduction have been studied for over last five decades; however, the detailed understanding of the drag reduction mechanism is still lacking. Vortices play an important role in turbulence structure. Nevertheless, the identification of vortices is still unclear, not even a universal definition of a vortex is accepted.

In the present study, several vortex feature extraction schemes are implemented. The methods are applied to analyze instantaneous two-dimensional velocity fields obtained by particle tracking Velocimetry (PTV) measurements of a turbulent channel flow with and without microbubble injection within the boundary layer. Microbubble injection is one of the drag reduction techniques, first studied in early 1970s, that has undergone extensive research in past years, and the generated information has aided into

drag reduction understanding.

As a general rule, vortex extraction methods can be either a simple visualization scheme or more sophisticated identification tools. The Reynolds decomposition and its variants are suitable due to their capacity to mark vortices advecting at different velocities. In the case of identification techniques, which yield a scalar field calculated from either the velocity vector field or the velocity gradient tensor, both the modified swirling strength Λ_{ci} or the λ_2 criteria were found to be well suited for vortex identification.

DEDICATION

This work is dedicated to Christian and Dulce.

ACKNOWLEDGMENTS

I cannot go ahead without expressing all my sincere indebtedness to my academic advisor and committee Co-Chair, Dr. Yassin A. Hassan. His fond guidance, unconditional trust and support, and endless patience and encouragement have been vital in any aspect of my career at Texas A&M University. He showed from the very beginning a superb willingness to help and advise me in whatever I do, clarifying all those concepts that happened to be obscure to me, while giving me the freedom I needed to study and work at a comfortable pace. Thanks to his very high standards, I stood up to date in a field that is continuously evolving, while having a broad overview of any issue related to my studies.

I would also like to acknowledge my other committee members, Dr. Kalyan Annamalai as Co-Chair, and Dr. William H. Marlow, and thank them for their prompt help in whatever I asked.

Lifelong thanks to the departments of Mechanical Engineering and Nuclear Engineering, and the NASA for their generous financial support during my postgraduate studies at Texas A&M University.

Lots of thanks to my co-workers and friends, Claudia del Carmen, Elvis Efren, Jose Alfredo, Ling Zhen, and Carlos Eduardo, for all their warm company and the disinterested help that meant the difference between being lost and learning. Also many thanks to my buddies and classmates, Carlos Ardenis and Joaquin Ivan, for standing by me anytime I needed them.

Genuine thanks to my parents and siblings, for their caring and support, and for encouraging me to excel in all aspects of my life.

Special gratitude to Dr. Luis San Andres, who made it possible for me to come to Texas A&M University.

TABLE OF CONTENTS

Page

ABSTRACT iii

DEDICATION v

ACKNOWLEDGMENTS vi

TABLE OF CONTENTS viii

LIST OF FIGURES x

LIST OF TABLES xii

1 INTRODUCTION 1

1.1 Turbulence Background 1
1.1.1 Basic Equations 2
1.1.2 Statistical Analysis 4
1.2 Turbulent Boundary Layers 7
1.3 Coherent Structures in Turbulent Boundary Layers 10
1.4 Vortex Detection 12

2 EXPERIMENT OUTLINE 17

2.1 Channel Flow Setup Test Facility 17
2.2 Particle Tracking Velocimetry (PTV) 20
2.2.1 Light Optics and Sources 20
2.2.2 Seeding Particles 23
2.2.3 Image Recording 26
2.3 Pressure Drop and Shear Stress 27
2.4 Microbubble Production and Void Fraction Measurement 29
2.5 Synchronization 31

3 PTV ANALYSIS AND FLOW CHARACTERIZATION 34

3.1 Measurement Process 34
3.2 PIV/PTV Analysis 35

Page

3.2.1 Image Pre-processing 35
3.2.2 Particle Tracking Velocimetry 36
3.2.3 Velocity Field Filtering and Interpolation 37
3.3 Main Flow Characteristics 38

4 VORTEX VISUALIZATION AND IDENTIFICATION 40

4.1 Vorticity 40
4.2 Galilean Decomposition 48
4.3 Reynolds Decomposition 52
4.4 Swirling Strength 55
4.5 Modified Swirling Strength 58
4.5.1 Vortex Statistics 62
4.6 λ_2 Criterion 66

5 SUMMARY 70

REFERENCES 72

VITA 77

LIST OF FIGURES

Page

Fig. 1.1. Sign convection for vortices 14

Fig. 2.1. Layout of channel flow experimental setup 19

Fig. 2.2. Lasers-cameras synchronization 22

Fig. 2.3. Optics setup 24

Fig. 2.4. Synchronization scheme 32

Fig. 4.1. Control volume mesh 42

Fig. 4.2. Instantaneous vorticity field **a** single phase flow; **b** α = 2.4%, DR = 12.9% 43

Fig. 4.3. Instantaneous vorticity field **a** α = 3.4%, DR = 16.1 %; **b** α = 4.4%, DR = 29.8 % 44

Fig. 4.4. Instantaneous vorticity field for α = 4.9%, DR = 38.2 % 45

Fig. 4.5. Time averaged vorticity field for **a** single phase flow; **b** α = 2.4%, DR = 12.9% 46

Fig. 4.6. Time averaged vorticity field for **a** α = 3.4%, DR = 29.8 %; **b** α = 4.4%, DR = 16.1 % 47

Fig. 4.7. Time averaged vorticity field for α = 4.9%, DR = 38.2 % 48

Fig. 4.8. Instantaneous vorticity and Galilean decomposed velocity field, single phase flow, $U_{adv} = 0.77\ U_b$; red arrow (+) vortex, blue arrow (-) vortex 49

Fig. 4.9. Instantaneous vorticity and Galilean decomposed velocity field, single phase flow, $U_{adv} = 0.83\ U_b$; red arrow (+) vortex, blue arrow (-) vortex 50

Fig. 4.10. Instantaneous vorticity and Galilean decomposed velocity field, single phase flow, **a** $U_{adv} = 0.88\ U_b$; **b** $U_{adv} = 0.95\ U_b$; red arrow (+) vortex, blue arrow (-) vortex 51

Page

Fig. 4.11. Instantaneous vorticity and Galilean decomposed velocity field, $\alpha = 4.9\%$, **a** $U_{adv} = 0.56\ U_b$; **b** $U_{adv} = 0.65\ U_b$; red arrow (+) vortex, blue arrow (-) vortex....53

Fig. 4.12. Instantaneous vorticity and Reynolds decomposed velocity field, **a** single phase, $f = 0.90$; **b** $\alpha = 4.9\%$, $f = 0.82$; red arrow (+) vortex, blue arrow (-) vortex....54

Fig. 4.13. Instantaneous λ_{ci} and velocity field, single phase, decomposed with **a** Galilean $U_{adv} = 0.83\ U_b$; **b** Reynolds $f = 0.90$; red arrow (+) vortex, blue arrow (-) vortex....57

Fig. 4.14. Instantaneous λ_{ci} and velocity field, $\alpha = 4.9\%$, decomposed with **a** Galilean $U_{adv} = 0.56\ U_b$; **b** Reynolds $f = 0.82$; red arrow (+) vortex, blue arrow (-) vortex....59

Fig. 4.15. Instantaneous Λ_{ci} and Galilean decomposed velocity field, single phase, $U_{adv} = 0.80\ U_{cl}$ **a** unfiltered; **b** filtered with RMS; red arrow (+) vortex, blue arrow (-) vortex....61

Fig. 4.16. Typical time averaged $RMS_{\Lambda_{ci}}$ showing the difference between considering Λ_{ci} as an unique signal and separating it into positive and a negative components....62

Fig. 4.17. Counting vortices from Fig. 4.15b....63

Fig. 4.18. Time averaged number of **a** positive; **b** negative vortices....64

Fig. 4.19. Time averaged area per positive vortex....65

Fig. 4.20. Time averaged area per negative vortex....66

Fig. 4.21. Time averaged swirling strength per **a** positive; **b** negative vortex....67

Fig. 4.22. Instantaneous λ_2 and Reynolds decomposed velocity fields **a** Single phase, $f = 0.98$; **b** $\alpha = 4.9\%$, $f = 0.82$....68

LIST OF TABLES

Page

Table 3.1. Average flow parameters for single and two-phase flows (water, 20 °C) 39

1 INTRODUCTION

In bounded turbulent flows, either internal or external ones, the regions closest to the wall are the most significant for both scientific and engineering reasons. It is in those regions where almost all the turbulence is generated, so they are birthplaces for phenomena of extreme practical importance such as drag, noise and vibration, mixing, transition, and separation. Fortunately, flows of different configurations, like channel flow or flat plate boundary layers, show in those innermost layers similarities that ease their research.

Given the limits that places on the study of turbulent flows their apparent randomness, it is natural the importance of the various coherent structures that have been found in turbulent boundary layers. Among those structures, vortices of different shapes are known to govern the turbulent processes and generate the other features. Thus it is imperative to develop a robust method to identify and measure those vortical structures in a flow field.

1.1 Turbulence Background

Although turbulence is almost omnipresent in natural flows and has significant importance in most fluid engineering applications, it is a subject that still raises many divisions among the scientific community. Thus, it is comprehensible that it is almost impossible to give turbulence a definition containing the major characteristics ascribed

---

This thesis follows the style of Experiments in Fluids.

to it by people working on different approaches to this problem.

In general, definitions of turbulence have regarded it as an irregular or random fluid motion (Hinze 1959; Bernard and Wallace 2002), whereas others have used a more up to date attribute of chaotic (Tsinober 2001), what is logic given the efforts to link the theory of Chaos with the study of turbulent flows (Tatsumi 1984). Irregularity and randomness, however, cannot be strictly considered qualities of turbulence, because of the presence of more or less coherent structures in those irregular motions (see, for example, Panton 1984). Moreover, it is universally accepted that even turbulent flows follow the equations of Navier-Stokes and continuity, thus they cannot be considered true random, but deterministic processes.

In contrast to its apparent randomness, well established and distinctive attributes of turbulence are that it is three-dimensional, rotational, and highly diffusive and dissipative. It also exhibits eddying motions, entrainment of turbulent-nonturbulent flows, and continuous spectra of all properties, dimensions and parameters. Eddies refer to any spatial/temporal structure or flow pattern that presents a high degree of correlation, and they are found in any shape and a continuous distribution of sizes.

1.1.1 Basic Equations

For flows that follow the conservation of mass principle, the continuity equation applies:

$$\frac{\partial \rho}{\partial t} + \nabla \cdot \left(\rho \mathbf{V} \right) = 0 \tag{1.1}$$

As it is stated above, it is accepted without any doubt that turbulent flows obey the Navier-Stokes equations, which for general Newtonian fluid flows is:

$$\rho\frac{\partial \mathbf{V}}{\partial t}+\rho\mathbf{V}\cdot\nabla\mathbf{V}=\nabla\cdot\left(-p\mathbf{I}\right)+2\nabla\cdot\left(\mu\left(\mathbf{D}-\frac{1}{3}\left(\nabla\cdot\mathbf{V}\right)\mathbf{I}\right)\right)+\rho\mathbf{g} \tag{1.2}$$

This, for incompressible flows, becomes:

$$\frac{\partial \mathbf{V}}{\partial t}+\mathbf{V}\cdot\nabla\mathbf{V}=-\frac{1}{\rho}\nabla p+\nu\Delta\mathbf{V}+\mathbf{g} \tag{1.3}$$

In equations 1.2 through 1.3, ρ, μ and ν are the fluid density, and the absolute and kinematic viscosities, respectively, p is the static pressure, **I** is the identity matrix, $\nabla\mathbf{V}$ is the velocity gradient tensor, $\nabla\cdot\mathbf{V}$ is the divergence of the velocity, $\Delta\mathbf{V}$ is the laplacian of the velocity, and **D** is the strain rate tensor, equal to the symmetric component of $\nabla\mathbf{V}$. The last values are defined in index notation by:

$$\nabla\mathbf{V}=\frac{\partial V_i}{\partial x_j} \tag{1.4}$$

$$\nabla\cdot\mathbf{V}=\frac{\partial V_i}{\partial x_i} \tag{1.5}$$

$$\Delta\mathbf{V}=\nabla^2\mathbf{V}=\frac{\partial^2 V_j}{\partial {x_i}^2} \tag{1.6}$$

$$\mathrm{D_{ij}}=\frac{1}{2}\left(\frac{\partial V_j}{\partial x_i}+\frac{\partial V_i}{\partial x_j}\right) \tag{1.7}$$

Another very important definition is the rotation or vorticity tensor $\mathbf{\Omega}$, equal to the antisymmetric component of $\nabla\mathbf{V}$:

$$\Omega_{ij} = \frac{1}{2}\left(\frac{\partial V_j}{\partial x_i} - \frac{\partial V_i}{\partial x_j}\right) \tag{1.8}$$

The three non-zero elements of $\mathbf{\Omega}$ constitute the vorticity vector $\boldsymbol{\omega}$:

$$\boldsymbol{\omega} = \left(\frac{\partial V_3}{\partial x_2} - \frac{\partial V_1}{\partial x_3}, \frac{\partial V_1}{\partial x_3} - \frac{\partial V_3}{\partial x_1}, \frac{\partial V_2}{\partial x_1} - \frac{\partial V_1}{\partial x_2}\right) \tag{1.9}$$

1.1.2 Statistical Analysis

The simplest and earliest mathematical tools applied to the theoretical study of turbulence and the analysis of turbulent experimental data come from Statistics (Reynolds 1895; Taylor 1935). Among those tools, averaging is the most common practice, and it can be done along independent samples, along a time series sampling, or along different spatial positions. Those possibilities are respectively called ensemble, time, and spatial averages, and defined for a random field $\mathbf{F}(\mathbf{x}, t)$ by:

$$\overline{\mathbf{F}}(\mathbf{x},t) = \frac{1}{N}\sum_{i=1}^{N}\mathbf{F}^i(\mathbf{x},t) \tag{1.10}$$

$$\overline{\mathbf{F}}(\mathbf{x},t) = \frac{1}{T}\int_{t-T/2}^{t+T/2}\mathbf{F}(\mathbf{x},t')dt' = \frac{1}{T}\sum_{i=1}^{N_T}\mathbf{F}(\mathbf{x},t_i)\Delta t_i \tag{1.11}$$

$$\overline{\mathbf{F}}(\mathbf{x},t)=\frac{1}{\mathbb{V}}\int_{\Pi}\mathbf{F}(\mathbf{x}',t)\,d\mathbb{V}=\frac{1}{\mathbb{V}}\sum_{i=1}^{N_{\mathbb{V}}}\mathbf{F}(\mathbf{x}_i',t)\,\Delta\mathbb{V} \tag{1.12}$$

$$\text{Where } \mathbb{V}=\int_{\Pi}d\mathbb{V}=\sum_{i=1}^{N_{\mathbb{V}}}\Delta\mathbb{V} \tag{1.13}$$

Here Π is the spatial region where the averaging is carried out. It could be a volume, a surface, or a curve, in which cases d$\mathbb{V}$ would be a differential of volume, area, or length, respectively.

The ensemble average, equation 1.10, is useful only for many independent samples. For few samples either temporal or spatial averages are more realistic, although temporal averages are useful only if **F**(**x**, *t*) is stationary or steady[a], that is, if its statistics are independent of time *t* and period *T* (Bernard and Wallace 2002; Rubin and Atkinson 2001). In this case, equations 10 and 11 will yield equivalent results for large time series data sets, i.e. large N_T.

In case of a variable *f* that oscillates around zero, the averages above defined could be equal to zero, thus giving an unrealistic depiction of *f*. In this case the root-mean-square (RMS) of the variable is preferred:

$$RMS(f)=\sqrt{\frac{\int P(f)f^2df}{\int P(f)df}} \tag{1.14}$$

Where *P(f)* in the probability distribution function of *f*, and the integrals can be done along any plane or path.

---

[a] Some authors use steady instead of stationary with the same idea (Schlichting and Gersten 2000)

Any physical variable in turbulent flow (it can be velocity, pressure, etc.) can be represented by the sum of an average component (any of the averages represented by equations 1.10 through 1.12 could in theory be applied, although the time average is the most used one) and a fluctuation:

$$\mathbf{V} = \overline{\mathbf{V}} + \mathbf{V}' \tag{1.15}$$

Reapplying the same averaging scheme to an averaged variable should give no different result (except for a small sampling, period, or spatial region). Therefore, averaging equation 1.15 yields $\overline{\mathbf{V}'} = 0$. This could give the false sensation that averaging would allow to get rid of fluctuations in any theoretical treatment of turbulent flows.

Nevertheless, the average of the product of any two components of **V**' will not always be zero; in effect, the covariance tensor of **V**, proportional to the Reynolds stress tensor[b], is:

$$R_{ij} = \overline{\mathbf{V}_i' \mathbf{V}_j'} \tag{1.16}$$

The Reynolds stress tensor $-\rho R_{ij}$ appears as an actual stress in the Reynolds averaged Navier-Stokes equation, that is, when equation 1.15 and a similar decomposition for pressure are inserted into equation 1.3:

$$\rho\left(\frac{\partial \overline{\mathbf{V}}}{\partial t} + \overline{\mathbf{V}} \cdot \nabla \overline{\mathbf{V}}\right) = \mu \Delta \overline{\mathbf{V}} - \left(\nabla \overline{p} + \rho \nabla \cdot \mathbf{R}\right) = \mu \Delta \overline{\mathbf{V}} - \nabla \cdot \left(\overline{p}\mathbf{I} + \rho \mathbf{R}\right) \tag{1.17}$$

Equation 16 can also be considered as the correlation tensor between the

[b] In most cases, R_{ij} is directly taken as the Reynolds stress tensor.

variables V_i' and V_j' at the same time and spatial position. A more general normalized correlation tensor can be calculated for velocities separated in space and time[c]:

$$R_{ij}(\mathbf{x},\mathbf{r},\tau) = \frac{\overline{\mathbf{V}_i'(\mathbf{x},t)\mathbf{V}_j'(\mathbf{x}+\mathbf{r},t+\tau)}}{\left(\overline{\left[\mathbf{V}_i'(\mathbf{x},t)\right]^2}\cdot\overline{\left[\mathbf{V}_j'(\mathbf{x}+\mathbf{r},t+\tau)\right]^2}\right)^{1/2}} \tag{1.18}$$

In the case $i = j$, the term autocorrelation is used for R_{ij}.

1.2 Turbulent Boundary Layers

In the study of turbulent boundary layers it is normal to consider them as divided into definite regions or sublayers, whose limits are given in terms of wall-normal dimensions. Those regions can also be grouped into an inner and an outer layers. Under certain assumptions, we can say that the characteristics of boundary layers, at least in their innermost levels, depend roughly on the wall-normal distance y, the wall shear stress τ_ω, and the fluid properties ρ and ν (Bradshaw et al. 1976). Thus a dimensional analysis would yield units for which different flow configurations would have compatible scales. First a friction velocity and the corresponding length scale are defined:

$$u_\tau = \left(\frac{\tau_\omega}{\rho}\right)^{1/2} \tag{1.19}$$

[c] Some authors just call this R_{ij} correlation or correlation coefficient, whereas others use this term to refer to the numerator of equation 1.18.

$$l_\tau = \frac{\nu}{u_\tau} \tag{1.20}$$

Those parameters allow us to scale velocity, space, and time:

$$u^+ = \frac{u}{u_\tau} \tag{1.21}$$

$$y^+ = \frac{y}{l_\tau} = y\frac{u_\tau}{\nu} \tag{1.22}$$

$$t^+ = t\frac{u_\tau}{l_\tau} = t\frac{u_\tau^2}{\nu} \tag{1.23}$$

It is also possible to define turbulent Reynolds numbers with those scales. For example, equation 1.22, which has the form of a Reynolds number, is actually the way this parameter is defined for pure turbulent boundary layers, i.e. those bounded by only one wall. For channel flows, the turbulent Reynolds number is given in terms of half the width (or height, if it is the smallest channel dimension), *h*:

$$\mathrm{Re}_\tau = \frac{u_\tau h}{\nu} \tag{1.24}$$

For outer sublayers it is more appropriate to scale spatial coordinates with the boundary layer thickness:

$$\eta = \frac{y}{\delta} \tag{1.25}$$

Back to channel flows, the length scale defined by equation 1.20 is usually

regarded as a wall layer thickness, δ, and redefined more conveniently in terms of Re_τ:

$$\delta = \frac{\nu}{u_\tau} = \frac{h}{\mathrm{Re}_\tau} \tag{1.26}$$

With those definitions in mind, it has been found that the inner layer is indeed split into an inmost sector, the linear or viscous sublayer, a buffer layer, and a logarithmic layer. The viscous sublayer extends from the wall up to about $y^+ \approx 3\sim8$. In this region, dereliction of the Reynolds stress term yields a highly accurate relation:

$$u^+ = y^+ \tag{1.27}$$

This viscous sublayer, though usually regarded as laminar or linear, has in reality shown some streamwise-elongated structures of low-speed flow called streaks (Kline and Robinson 1988).

The buffer layer, which extends from about $y^+ \approx 3\sim8$ to around 40, is where most turbulence is produced. In this region, no practical expression for the mean velocity could be theoretically obtained, in part because both viscous and Reynolds shear stresses are essentially of the same order of magnitude.

In the logarithmic layer, also called intermediate or overlap layer, Reynolds shear stresses are much stronger than the viscous term in equation 1.17. A dimensional analysis similar than the one performed to get equation 1.26 for the viscous sublayer yields:

$$u^+ = \frac{1}{\kappa}\ln\left(y^+\right) + C \tag{1.28}$$

Where κ, called the Karman constant, was experimentally found to be around 0.41. This relation represents very accurately the mean velocity, even with small deviations from the zero pressure gradient, in the extent of the intermediate layer, that is from $y^+ \approx 40$ up to around $\frac{y}{\delta} \approx 0.2$ (Bradshaw et al. 1976). Nonetheless, a more realistic and exact power law has been proposed for this region (Barenblatt et al. 1997).

The outer layer, which covers about the upper 80 % of the turbulent boundary layer, is distinguished by the frequent and irregular entrainment of non-turbulent external flow by turbulent fluid from the outer edge of the boundary layer.

1.3 Coherent Structures in Turbulent Boundary Layers

It was not after the first half of the twentieth century that the experimental techniques applied to the study of turbulent flows gave enough evidences that organizations of spatially and temporally coherent patterns existed inside the apparently randomness of turbulent flows. Meticulous experimental results (see, for example, Laufer 1953; Klebanoff 1954; Corrsin and Kistler 1954; Hanratty 1956) during the 1950s allowed the identification and portrayal of the main regions and sublayers present in a turbulent boundary layer, as well as the most perceptible structures, like the low and high-speed streaks. However, the first suggestion of a coherent structure (CS) in wall turbulence ironically corresponds to Theodorsen's (Theodorsen 1952) hypothesis of a horsehoe-shaped vortex, which turned out to be the most difficult structure to visualize and measure in laboratory. Further supporting studies were presented giving vortices and

vortical structures[d] a significance even higher than that of other CS (Townsend 1956; Runstadler et al. 1963).

The Reynolds stress $-\rho R_{ij}$ is a very important turbulence parameter because of its direct relation to skin friction and drag (Gutierrez Torres 2004). In order to identify processes that contribute to higher Reynolds stresses, the quadrant method has been applied (Wallace et al. 1972; Willmarth and Lu 1972). In this analysis, the instantaneous velocity product that make up equation 1.16 ($u'v'$ for 2D streamwise wall-normal velocity field) is classified into four groups or quadrants depending on the signs of the velocities: Q_1 ($u' > 0$, $v' > 0$), Q_2 ($u' < 0$, $v' > 0$), Q_3 ($u' < 0$, $v' < 0$), Q_4 ($u' > 0$, $v' < 0$). These quadrants are associated to specific events or structures, being of major importance those directly linked to negative shear stress $u'v'$: Q_2 is related to ejections, and Q_4 to sweeps.

Ejections, which are part of the burst phenomenon, occur when low-speed streaks move quickly away from the wall, whereas sweeps refer to inrushes towards the wall of high speed flow from the intermediate layer. Although both structures necessarily entail each other, and are main responsible of Reynolds stress generation near the wall (Kline and Robinson 1988), sweeps produce most of Reynolds stresses for $y^+ < 12 \sim 15$, whereas ejections dominate that production above that zone.

Vortices are regarded today as the dominant structure in near wall turbulence and skin friction production (Schoppa and Hussain 1998, 2002). Furthermore, most other structures can be explained as result of the behavior of vortices (Bernard and Wallace

[d] Hairpin, horseshoe, or vortical structure will have along this thesis the same meaning, that is a complete or partial Λ–like structure having properties of a vortex.

2002; Zhou et al. 1999). The great drawback in vortical structures is their identification, since even a universal and accurate definition of vortex is lacking.

1.4 Vortex Detection

The most popular notion of a vortex is probably the vortex tube or filament, which encloses fluid rotating around an axis tangent to the vorticity vector (see Lamb 1932). In fact, the notion of vortices is one of the oldest concepts in fluid mechanics, and many different cases have been theoretically studied, and even visualized in laboratory, for more than one century (Lamb 1932; Taylor 1923; Hill 1894). Nevertheless it has been quite difficult to quantitatively determine vortical structures with existing laboratory techniques (Kline and Robinson 1988).

It was with early flow visualization methods (dye tracers, hydrogen bubbles, etc.) that the first attempts to identify vortices were made (for example, by looking for closed or spiral streaklines or streamlines), though they quickly proved to be ambiguous in many cases (Jeong and Hussain 1995; Adrian et al. 2000). The local pressure minimum on the vortex axis, another instinctively conceived, basic criterion, is supported by the idea that pressure and centrifugal forces are in equilibrium in the core. However, this definition of vortex core has also been shown to be inadequate (Jeong and Hussain 1995).

The longest-established vortex identification process has so far been the utilization of the vorticity magnitude $\|\boldsymbol{\omega}\|$ to represent vortex loci. Amidst its advantages are its computational simplicity, its successful application to simple flow fields with

little or no shear, and its direct association with multi-point measurement techniques, like Particle Imaging Velocimetry (PIV), Laser Speckle Velocimetry (LSV), or Doppler Global Velocimetry (DGV). Its main weakness is, however, its inability to reveal vortex cores in presence of flow regions where the shear is so strong that their vorticity magnitudes are comparable to those of the actual vortices (Jeong and Hussain 1995).

Schemes to recognize vortices based on velocity field can be classified into frame independent and frame dependent[e], depending on how their results depend on the reference frame chosen for the analysis of that field. For instance, the vorticity criterion is frame independent, whereas the streaklines or streamlines methods are dependent. Three relatively new Galilean invariant vortex identification techniques have been proposed, which depend either on the eigenvalues of the velocity gradient tensor $\nabla\mathbf{u}$ (Chong, et al. 1990; Zhou et al. 1996, 1999), the second invariant of the velocity gradient tensor (Hunt et al. 1988), or the Hessian of pressure, based on the eigenvalues of a portion of the symmetric component of the acceleration gradient tensor $\nabla\mathbf{a}$ (Jeong and Hussain 1995).

When the discriminant of the characteristic equation of a three-dimensional velocity gradient tensor $\nabla\mathbf{u}$ is positive, this latter has complex eigenvalues, one real and two complex conjugate (λ_r and $\lambda_{cr} \pm i\lambda_{ci}$, respectively). Chong et al. (1990) proved that in this case the flow streamlines around a point, in a reference frame moving with the point, have closed or spiral shapes. It can be shown that λ_{ci} measures how strongly the vortex swirls (it is its actual frequency of rotation about its axis), and actually it was named

[e] In some papers this is equivalent to Galilean invariant and non invariant (Jeong and Hussain, 1995)

"swirling strength" (Zhou et al. 1999). The swirling strength method has also been adapted to two-dimensional velocity field measurements by looking for points where the plane velocity field gradient tensor has two complex eigenvalues (Adrian et al. 2000). Although this process has proved its robustness, it has a disadvantage compared to the vorticity mapping, i.e., it does not reveal the direction of rotation, so Christensen and Wu (2004) proposed a modified swirling strength, by combining λ_{ci} with $\|\boldsymbol{\omega}\|$:

$$\Lambda_{ci}(x,y) = \lambda_{ci}(x,y) \cdot sign\left(\boldsymbol{\omega}_z(x,y)\right) \tag{1.29}$$

Positive and negative values of Λ_{ci} will indicate the presence of counter and clockwise rotation, respectively, whenever observed in a right-handed coordinate system as shown in fig. 1.1.

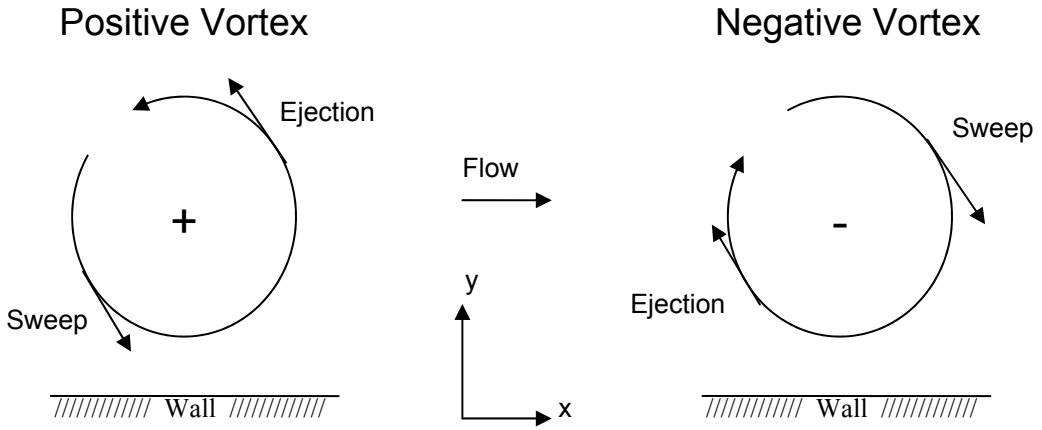

Fig. 1.1. Sign convection for vortices

Jeong and Hussain (1995) solved for the Hessian of pressure from the symmetric component of the gradient of the Navier-Stokes equations and disregarded the

contributions of the terms representing the unsteady irrotational straining and viscous effects, resulting in a symmetric tensor, $\mathbf{S}^2 + \mathbf{\Omega}^2$, where $\mathbf{S}$ and $\mathbf{\Omega}$ are the symmetric and antisymmetric parts of the velocity gradient tensor $\nabla\mathbf{u}$, respectively. Then they defined a vortex core as "a connected region with two negative eigenvalues of $\mathbf{S}^2 + \mathbf{\Omega}^2$".

Hunt et al. (1988) considered the second invariant Q of the velocity gradient tensor $\nabla\mathbf{u}$ as an indicator for 'eddies', and defined a vortex as a region with $Q > 0$. It can be seen that Q denotes a local equilibrium between shear strain and vorticity from its definition:

$$Q = \frac{\|\mathbf{\Omega}\|^2 - \|\mathbf{S}\|^2}{2} \tag{1.30}$$

So far, methods have solely relied on the velocity field and its related tensors. A criterion that depends on pressure comes from the fact that a vortex core, or the axis of any swirling motion, tends to coincide with a local pressure minimum because inertial and pressure forces tend to cancel each other. Although it has been applied with certain success (Robinson et al. 1988), it must be pointed out that it requires the careful choice of a reference pressure. This method will no be applied in this work because a pressure field has not been measured.

Unlike vortex identification schemes, visualization techniques do not offer a trigger value to indicate the location of a vortex, but depend on the researcher's criterion and capacity to discern when a vector field pattern looks like a vortex, usually applying the Kline and Robinson definition (Robinson et al. 1988). Traditionally, it was the Reynolds decomposition of the velocity field into an average mean $\mathbf{U}$ and velocity

fluctuations **u** the standard scheme to visualize turbulent flows. However, this is not the best available method to look for structures of specific scales, mainly small and large eddies (Adrian et al. 2000). Different from Reynolds decomposition, which subtract an either space or time dependant average mean **U** to the instantaneous velocity fields, Galilean decomposition takes a constant convection velocity, $\mathbf{U_c}$, out of the field, and this convection velocity can be freely chosen, though it seldom depends on space variables. LES decomposition techniques, which include the proper orthogonal decomposition (POD), have been used with slightly better results (Liu et al. 2001; Adrian et al. 2000), though they are computational more complicated. Recently, a modified Reynolds decomposition and a spatial decomposition were successfully applied to turbulent single phase and microbubble injected channel flows (Gutierrez Torres 2004).

2 EXPERIMENT OUTLINE

Instantaneous two-dimensional velocity fields were measured on the streamwise-wall-normal plane in a turbulent channel flow by means of the Particle Tracking Velocimetry technique. Both single and two-phase flows, consisting on water and water-microbubbles at different void fractions, were considered. The velocimetry realizations were synchronously accompanied with pressure drop measurements, and these latter were verified with assessments of wall shear stress with an optical device.

2.1 Channel Flow Setup Test Facility

The main part of this facility is a Plexiglas-made tunnel of rectangular section and a constant width of 20.5 cm (8”), as is shown in fig. 2.1. Unlike its inlet nozzle and outlet diffuser, its 4 m (13 ft 1”) long central segment has a constant 5.6 cm (2.2”) height. Its 12.7 mm (0.5”) thick walls allow us to work with quite high pressures.

The water flow cycle starts at a 90-gallons lower tank, which is the ground level and acts as a reservoir. It contains three submerged pumps, rated at 1/2, 1/4, and 1/6 HP, that provide, by different combinations, a wide gamma of flow rates. These pumps send water to a 54-gallons upper tank, placed 285 cm (9 ft 4”) above the reservoir. This tank contains an internal leveler, basically a concentric cylinder that keeps constant the water level by sending the overflow back to the phase separator tank. This way, constant flow rate and pressure head are assured by keeping a regular excess returning to the lower tanks. This internal leveler works also as a phase separator that keeps water free from air

bubbles. When full, the upper tank supplies with a constant pressure of 3.65 m (11 ft 11 ¾ “) of water and a flow rate up to a maximum of 41.3 GPM.

The channel inlet is connected to the base of the upper tank through three hoses (two 1 ¼ “ and one 1” diameter). The flow rate entering the channel is measured with one floating-ball (0~10 GPM) and two magnetic-digital (0~50 GPM) flow meters working in parallel, while three throttles allow to control the total flow rate.

An inlet nozzle and an outlet diffuser, also Plexiglas-made, add another 83 cm (33”) to the channel length. A flow straightener consisting on a plastic straw is placed at the entrance of the inlet nozzle to achieve a uniform 2-dimensional flow. Fully developed flow condition is attained by placing the measurement section some 2.8 m (110”) after the beginning of the constant cross-section sector.

Intakes for the differential pressure manometer are drilled on the channel upper face at 135, 58.4, and 2.54 cm (53”, 23”, and 1”, respectively) upstream, and 17.8 and 94 cm (7” and 37”, respectively) downstream the test section. Other holes are made for the optical shear stress sensor, 2.54 cm (1”) downstream the measurement zone, and for the microbubble generator, around 5.08 and 7.62 cm (2 and 3 “, respectively) upstream.

The outlet diffuser discharges into the phase separation tank through a set of hoses like those that feed the channel. The phase separator, placed at the same level as the reservoir tank and connected to it through tubes, perform the removal of air bubbles trapped in the water flow, while damping most of turbulence so that the pumps tank receive a calmer flow.

A. Upper Tank.
B. Flow Meters.
C. Throttles.
D. Plastic Screen.
E. Channel Inlet.
F. Pressure Transducer.
G. Microbubbles Generator.
H. Laser Sheet.
I. Measurement Zone.
J. Channel Outlet.
K. High Resolution Camera.
L. CMOS Cameras.
M. Pressure Intakes.
N. Beam Splitter.
O. Phase Separator.
P. Lower Tank.
Q. 1/2, 1/4, and 1/6 HP Pumps.
R. Microbubles.
S. Nd:Yag Laser.
T. Lens.
U. Mirrors.
V. Overflow Return.

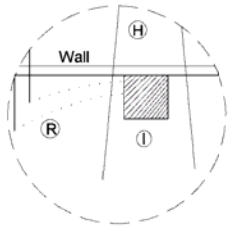

Detail A

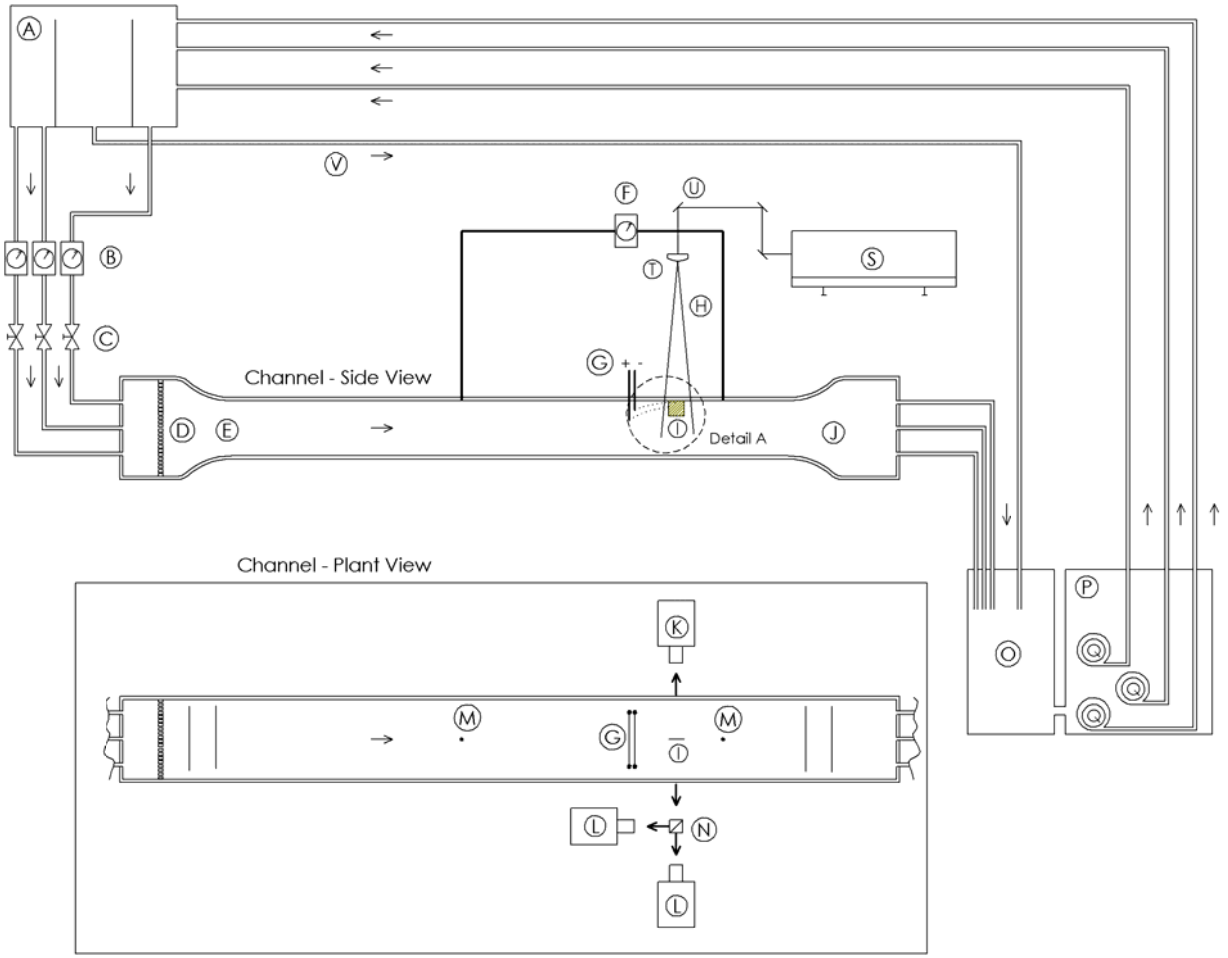

Figure 2.1. Layout of channel flow experimental setup.

2.2 Particle Tracking Velocimetry (PTV)

Particle Tracking Velocimetry, a variant of Particle Image Velocimetry (PIV), differs from it, from a physical point of view, only on the density of images of tracer particles. However, the analysis algorithms are quite different, since in PTV, individual particles can be identified and tracked, whereas in PIV, statistical analysis must be applied.

PIV and PTV are basically non-intrusive 2-D whole-field flow velocity measuring techniques based on optics. The working fluid is seeded with uniformly sized and shaped small particles that reflect and scatter monochromatic light of a laser sheet. That reflected light is collect by a camera to form an image that is then digitalized.

2.2.1 Light Optics and Sources

Because PIV/PTV normally provide only the velocity components on the plane of the light sheet, it must be as thin as possible to guarantee that particles crossing that plane will be disregarded. However, this implies a compromise when low particle concentrations are employed. Also, the light source must be pulsed in intervals of time short enough to avoid blurring of the images. Lasers are preferred over white light because their monochromatic radiation allow to create light sheets without chromatic aberration, and their high energy density provide those sheets with the power necessary for the visualization of the smallest particles during very short pulses.

Lasers can be based either on a electrically ionized molecular gas, an optically pumped solid-state crystal rod, or a light emitter semiconductor. Among the first group

the most popular are the helium-neon lasers, He-Ne, which supply with a red light of λ = 633 nm with an outstanding efficiency. In this group we also find the argon-ion lasers, Ar^{+}, which require very high currents to provide their multiple wavelengths in the green-blue and ultraviolet ranges, being the most important 488.0 and 514.5 nm. Unlike these lasers, which require intensive cooling, copper-vapor lasers (Cu, λ = 510 and 578 nm) need high temperatures and thermal insulation because they involve vaporization of cupper.

Optically pumped lasers are the oldest concept in laser science. The first lasers were the ruby lasers, also called Cr^{3+}, with a red wavelength of λ = 694 nm. The most widely used lasers in PIV/PTV are the neodymium-YAG lasers, in which Nd^{3+} ions introduced into a matrix of yttrium-aluminum-garnet produce a beam at λ = 532 and 1064 nm. The first wavelength is the only used for PIV/PTV, though it has around one half the energy of the other frequency. The main advantage of semiconductor lasers is their compactness, but they increase considerably equipment prices.

For the experiments related to this work, the light source was a Spectra-Physics Quanta-Ray Nd-YAG twin-laser that supplied with a 350 mJ/pulse green radiation of wavelength λ = 532 nm. The laser beams, called 1 and 2 in fig. 2.2, were synchronized to shoot pairs of 7 ns pulses (one pulse per laser) separated by 1 ms. The frequency of pairs was equal to the camera maximum frame rate.

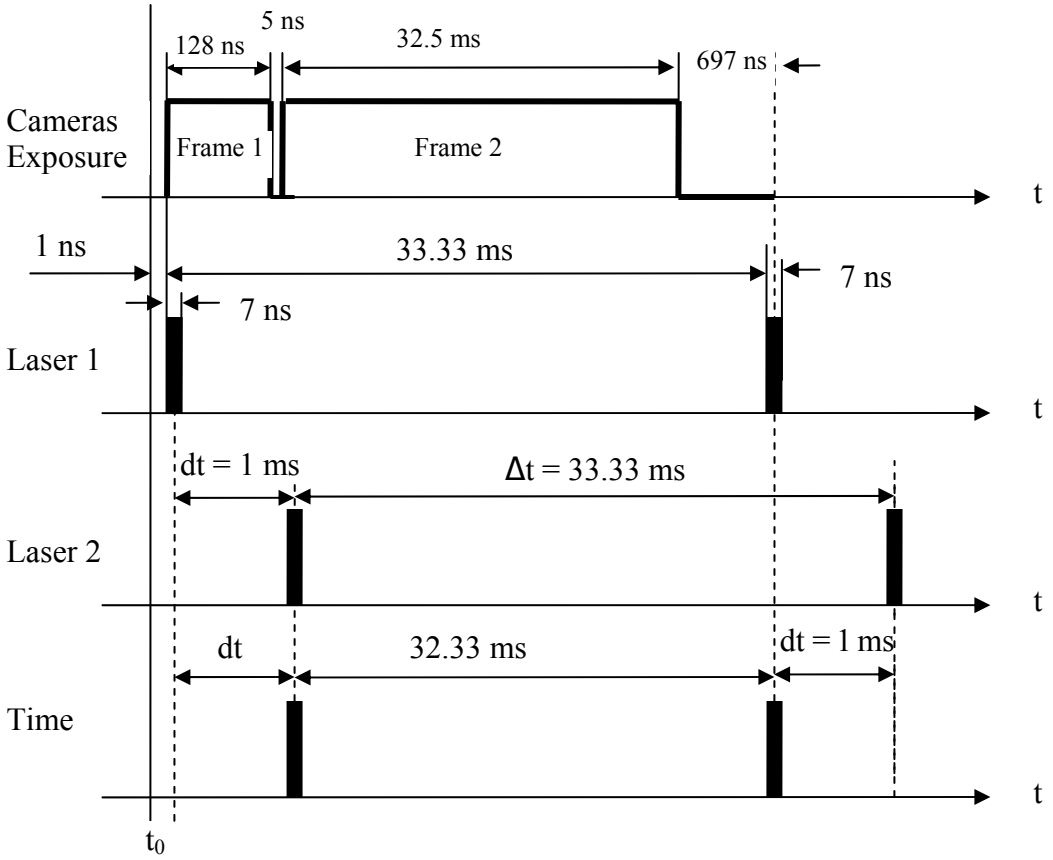

Fig. 2.2. Lasers-cameras synchronization

Most of the optics in PIV/PTV cover the generation of the light sheet, what is typically done with row configurations of two or three lenses. In either case cylindrical lenses (with a constant curved section along an axis) are set in linear arrangements to yield a light sheet of appropriate width and thickness, although combinations with spherical lenses are also possible (for more information on PIV optics, see Raffel et al. 1998). Setups are usually completed with mirrors and prisms of total or partial reflectivity.

The optical system assembled for the experiments related to this work consisted

on three mirrors (one with 50% of reflectivity) capable of enduring high-energy laser beams, two cylindrical lens (focal length = 10 and 20 cm) that generate a 1 mm thick diverging light sheet that crosses vertically the channel from top to bottom in the mid span, and a beam splitter containing a prism, as shown in fig. 2.3.

2.2.2 Seeding Particles

The most important issues concerning the flow seeding are the particle-fluid density matching, light scattering, and particle supply. The success of the velocity measurement depends upon the capacity of the particle to follow the fluid motion, and it is indispensable that the inertial and gravitational forces acting on the particle and fluid be similar to avoid discrepancies between their velocities. The simplest physical analysis gives the gravitationally induced velocity for spherical particles:

$$u_g = \frac{2R_P^2 g}{9\mu}\left(\rho_P - \rho\right) \tag{2.1}$$

Here R_P and ρ_P are the particle radius and density, respectively, g is gravity, and μ is the fluid viscosity. It is clear that, for a given fluid, this velocity will decrease for either smaller particles or a better matching between the densities. For inertial forces the same analysis is applicable, but with the fluid acceleration instead of gravity.

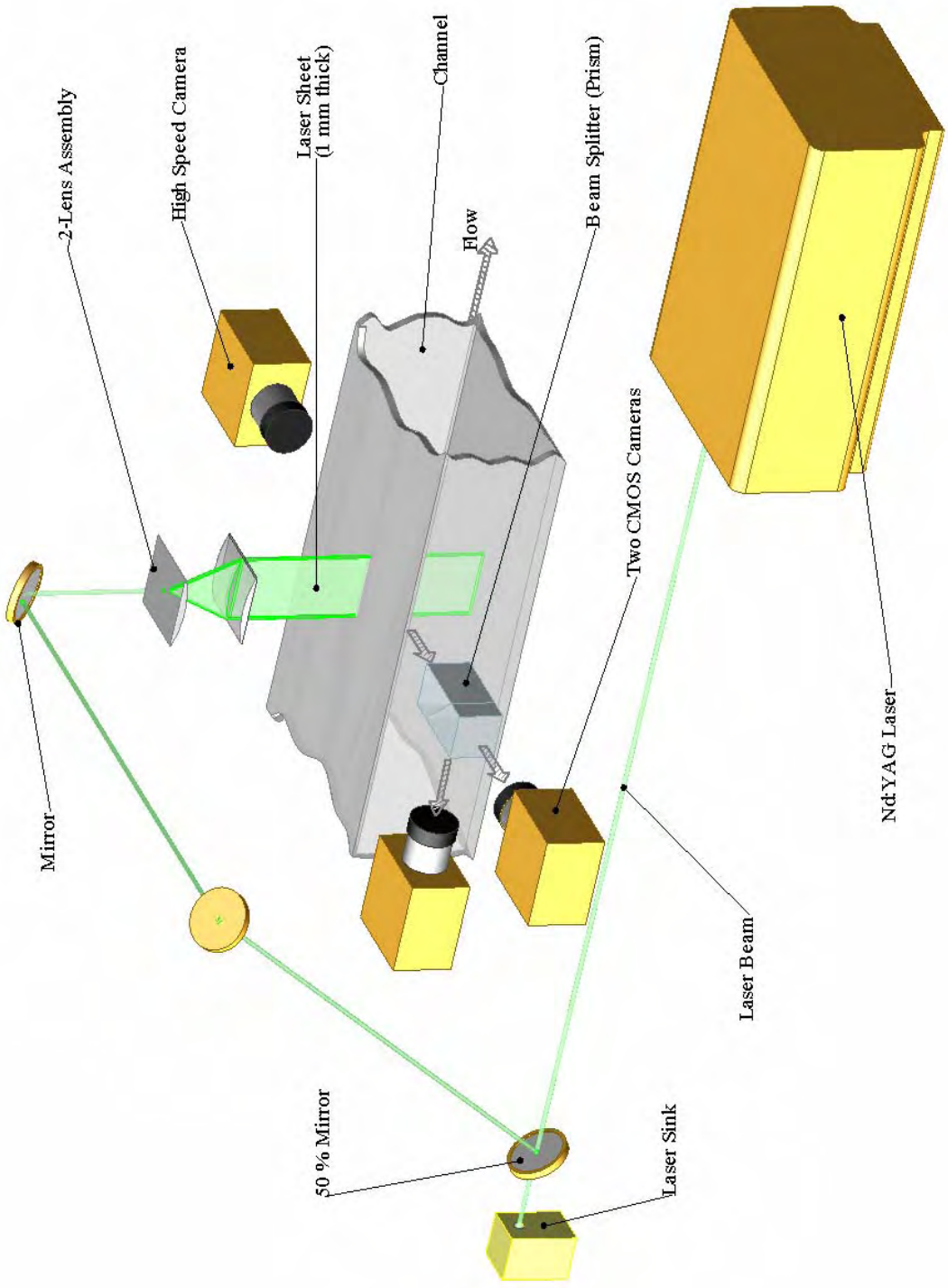

Fig. 2.3. Optics setup

The light that a small particle scatters is normally a function of its size, shape and orientation, and the ratio of its refractive index and that of the fluid. The scattered power increases with increasing particle size and, for particles with diameter larger than the light wavelength, Mie's scattering theory establishes that the intensity is approximately proportional to the square diameter (van de Hulst 1981). Thus there is a clash between the constraints of light scattering and velocity matchings that the experimentalist must balance.

The seed particles can be naturally present in the flow stream, or introduced either during the experiment, or, prior to it, mixed with the fluid. The first case is acceptable only when the particle sizes and concentration meet the requirements for the experiment. For liquid flows in closed-loop circuits, solid particles are normally homogeneously mixed with the fluid at a certain point of the loop, almost always a tank. This was the case in the experiments of this work, in which particles (model Expancel 091DU) with an average diameter of 6 μm, a specific gravity of 1.05, and a refraction index suitable for PIV were used.

Gas flows are generally seeded with liquid droplets by using aerosol generators placed upstream the test section. As it was stated above, it is important to take care of the particle concentration or density, since it will determine if individual particles can be identified in two successive images. Thus it is possible for low particle concentrations and flow velocities that particle separations be larger than their displacements between images, so single particles could be tracked. This is the base of Particle Tracking Velocimetry. Its main disadvantage is that it can only reveal flow structures whose size

is of the order of the mean distance between particles, so it is more appropriate for low Reynolds numbers.

2.2.3 Image Recording

Photographic recording and CCD (Charge Coupled Devices) cameras are the two technologies most used so far for PIV/PTV recording. Photographic films provide the best resolutions and image quality, but their setup is more difficult and the development is very expensive and time consuming. Semiconductor based CCD cameras, in contrast, represent a field in continuous evolution, and became in late1980s affordable devices with resolution and contrast suitable for most applications. Although digital technology still offers spatial resolutions that are around two orders of magnitude lower than those that can be obtained with films, modern resolutions allow to solve a wide range of turbulent length scales.

A particle displacement can be record either by capturing two or more positions in a single picture (single frame/multiple exposure), or a picture per light pulse (multiple frame/single exposure), allowing this latter to solve the directional ambiguity. CCD cameras are more suitable for the second method, because they can be shot at variable intervals, whereas single frame/multiple exposure has been traditionally used with photographic techniques. For a more detailed description of recording technologies, see Dominguez Ontiveros 2004.

Two Panasonic GPMF702 cameras, with a resolution of 640x480 pixels (13.5x13.5 μm each one) and a frame rates of 30-60 fps, recorded from a beam splitter

and provided an analog output to a National Instruments PCI 1408 frame grabber. The frame grabber contained four independent AD converters and a synchronization circuitry. One Kodak Megaplus E.S. 1.0 camera, with a resolution of 1008x1008 pixels (9 μm each one) and a normal frame rate of 30 fps, recorded from the opposite side of the channel and provided a digital output to a National Instruments PCI 1424 frame grabber. This last camera allowed a maximum frame rate of 60 fps by using a triggered double exposure technique. All cameras had CCD arrays of the type FFIT (Full Frame Interline Transfer) and were configured at 256 gray scales (8 bits).

The reason for using those cameras is that the high speed and resolution Megaplus E.S. 1.0 was set up to record mainly the inner layer and part of the outer, while paying attention to small temporal scales. The CMOS cameras, on the other hand, were aimed at the average characteristics of the flow field, though they were focused on areas of different size.

2.3 Pressure Drop and Shear Stress

A Validyne DP103 differential pressure transducer was used to measure the static pressure difference between an upstream point in the channel and a downstream point. It was assumed that this static pressure does not change along the wall-normal direction from the wall. This device is based on a diaphragm and a variable reluctance coil, whose impedance changes proportionally to the diaphragm deformation.

The pressure transducer was placed in the midpoint between the intake tabs closest to the measurement zone on the upper wall of the channel. With the usual

assumptions of symmetric plane channel flow under constant pressure gradient ∇P, a simple relationship between this one and the wall shear stress τ_ω can be derived (Durst et al. 1996):

$$\tau_\omega = -h\frac{dP}{dx} \tag{2.2}$$

Where h is the channel half height and $\frac{dP}{dx}$ is the pressure gradient approximated by the drop between the tabs, separated by about 23 cm. For Newtonian fluids, assuming non-slip and other conditions, there is a link between τ_ω and the wall-normal component of the velocity gradient:

$$\tau_\omega = \mu\left.\frac{dU}{dy}\right|_{y=0} \tag{2.3}$$

With this shear stress all non-dimensional parameters in section 1.2.3 can be calculated.

To verify the shear stress calculated from pressure drop, direct measurements were performed with an optical shear stress sensor, but they could not be simultaneous to the pressure and velocity assessments because the high energy Nd:YAG laser would have tampered the shear stress measurements and even damaged the optical sensor. This technique, based on the Divergence Fringe Doppler principle, required that a photo detector be mounted on the top wall close downstream the test section, while a laser beam divided in radial fringes was pointed through that section. It is important to note

that that laser was required to have very different features than those of the Nd:YAG, like a larger wavelength and a lower energy. Thus those measurements were carried out immediately after turning off the Nd:YAG laser while keeping the flow stabilized and the pressure sensor still reading. This way, the optical stress measurements could be corroborated.

2.4 Microbubble Production and Void Fraction Measurement

Two parallel 5.5 cm long Platinum wires of diameter 76 μm were positioned horizontal and normal to the flow just upstream the test section at the same spanwise location, that is, in the middle of the channel width (see fig. 2.1). Although the wires were actually longer, the rest of them was electrically insulated, so only a central portion was really in contact with the water. They acted as electrolysis electrodes to generate Hydrogen-Oxygen microbubbles. The cathode or negative electrode, responsible for the Hydrogen generation, was 11.45 cm (4.5“) upstream the center of the test section and 0.5 cm (0.2”) below the upper wall. The anode, where Oxygen was produced, was 13.99 cm (5.5”) upstream the center of the test section and 1.5 cm (0.2”) below the upper wall. The difference in *y*-positions of the wires responds to the necessity to keep the bubbles precedent from both electrodes separated, and those originated at the anode away from the test section. Their distances to the test section were more than one thousand times the wire diameter, so its effect on the flow te be measured was negligible.

The wires were provided with a regulated 12 V DC voltage rated at 25 mA. The Faraday’s Law of Electrolysis gives a very accurate approximation of the element mass

production by electrolysis at either cathode or anode (Gutierrez Torres 2004):

$$\dot{m}_H = 7.11 \times 10^{-10} \frac{I \cdot w}{z} \tag{2.4}$$

Here I is the current in amperes, and w and z are the element atomic weight and valence number, respectively. For the Hydrogen, w = 1.008 and z = +1. The average microbubble diameter for those conditions was around 30 μm.

Instantaneous void fractions on the streamwise wall-normal plane (x-y plane) were assessed by using the shadowgraphy technique, in which a collimated uniform light beam that covers the entire test section crosses it normally in spanwise direction thus revealing the bubbles by differences in refractive indices. A plane light source was made up of LEDs, placed on one side of the channel, and triggered in synchronism with the camera, located on the other side. The reason of using LEDs instead of the laser was that this latter was too powerful and could have permanently damaged the CCD element of the camera. The image processing provided with the bubble areas, which in turn are directly related to their volumes, V_b. A relation between bubble and water volumes gives the void fraction α:

$$\alpha = \frac{V_b}{V_b + V_f} \tag{2.5}$$

Where V_f is the fluid volume.

2.5 Synchronization

In experimental studies of turbulence, it is imperative to perform to measure as many flow parameters as possible, and to make all those measurements accurately defined in a unique time frame. This last requirement is met by a correct synchronization between the various instruments involved in the measurement, as is shown in fig. 2.4.

The illumination, pressure transducer sensor, and the three cameras were synchronized by a Stanford Research DG535 high accuracy pulse generator, which can deliver user programmed digital signals through his five output channels A, B, C, D, and E. In this specific case, the pulse generator was programmed to give 30 Hz signals.

As stated above, the Nd:YAG laser has twin lamps that provide with two independent laser beams that share the same wavelength and path, although they can be triggered at different times, thus allowing to be used separately. The lamps corresponding to laser beams 1 and 2 received from the DG535 output channels A and C, respectively, independent TTL (Transistor-Transistor Logic) pulses through their respective inputs in the laser unit. As can be seen in fig. 2.2, channel A was programmed to provide with a 7 ns square pulse, and channel C was delayed by 1 ms, which was the PIV time differential, *dt*.

Related to signals A and C were the time exposures of the high speed camera, which was programmed to operate, driven by channel D, in a triggered double-exposure mode that provided with the maximum frame rate of 60 fps. In this mode, the camera can shot pairs of pictures separated by a fixed time interval of 32.5 ms, so 30 pairs of images can be recorded per second. In each pair, the photographs are separated by a

minimum delay of 0.133 ms, which, after deducting the 5 ns needed for image transfer, yields an exposure time of 0.128 ms for the frame 1 (see fig. 2.2). This, along with the fact that frame 2 can be exposed as much as 32.5 ms, constitute the main drawback of this method. On the other hand, the strobe output of the high resolution camera was taken as a triggering signal for the shadowgraphy LED panel.

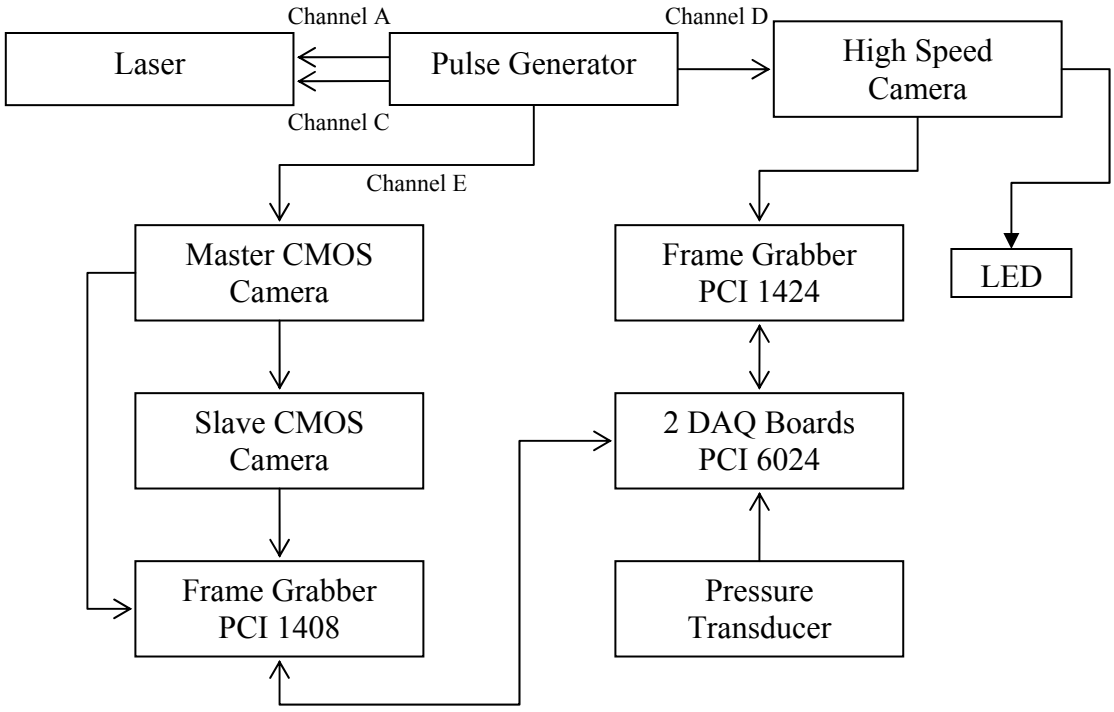

Fig. 2.4. Synchronization scheme

The frame grabber PCI 1424 that took the digital signal from the Megaplus E.S. 1.0 high speed camera into the computer was driven by a LabVIEW program, and generated the trigger signal that activated the data acquisition from the pressure transducer. This data acquisition was performed by two NI PCI 6024 boards that AD

converted the analog signal supplied by the pressure sensor.

The channel E of the pulse generator provided the trigger signal for one of the two CMOS cameras, which, working as a master device, generated with its own internal clock a pulse train that triggered the slave CMOS camera, so they were synchronized. The channel E was programmed taking into account a small delay produced in that synchronization.

3 PTV ANALYSIS AND FLOW CHARACTERIZATION

As mentioned in previous section, instantaneous two-dimensional velocity fields along the channel's streamwise-wall-normal plane of symmetry were obtained by means of PTV technique. As a convention, if the streamwise and wall-normal positions are given by $x \cdot \mathbf{e_1}$ and $y \cdot \mathbf{e_2}$, respectively, the velocity field is $\vec{\mathbf{V}} = u \cdot \mathbf{e_1} + v \cdot \mathbf{e_2}$. In addition, Direct and indirect measurements of wall shear stress τ_w were carried out, as well as estimations of liquid-gas void fractions α.

3.1 Measurement Process

Twenty sets of 100 pairs of images were taken with the high speed camera, while being the flow stabilized at a flow rate $\dot{\mathbf{V}} = 33$ GPM and a Reynolds number $Re_h = 5128$, based on the bulk velocity U_b and the half height of the channel h. Since the turbulent flow was completely developed, U_b was calculated simply from $\dot{\mathbf{V}}$ and the channel cross section, $A = 114.8$ cm^2:

$$U_b = \frac{\dot{V}}{A} = 18.13 \frac{cm}{s} \tag{3.1}$$

The Megaplus E.S. 1.0 camera was focused on a 11.31×11.31 mm square area abut the upper wall and each set spanned 3.3 sec. Ten sets involved single phase flow, i.e. no bubble production. In the other ten sets the void fraction α was continuously increased along samples, though it was assumed constant during each set because of

their short time extent (3.3 seconds) compared to the 30-60 sec between them. The actual void fractions had been previously measured on a rectangular zone six test sections long by using shadowgraphy and applying equation 2.5. For single phase cases, pressure measurements were performed at 1 KHz, although because of data storage constraints, they were not made simultaneous to velocity and shear stress samplings.

Optical measurements of wall shear stress, 1000-sample long each one, were made after every set of images, with the Nd:YAG laser turned off. Because of the optical obstruction caused by the accumulation of microbubbles on the upper wall, the sensor was run for two-phase only at the beginning of the microbubble production.

3.2 PIV/PTV Analysis

The images coming from the cameras were saved as 256-grayscale 1008×1008 bitmap files. Those images contained undesirable noise as a natural result of a measurement process, and its most important causes were the background laser radiation and the strong light scattering and reflection close to the wall. Therefore, the first step after the measurements was to remove that noise.

3.2.1 Image Pre-processing

To remove all that noise, those images were pre-processed by carrying out a filtering, consistent in time averaging a whole sample (all samples were made up of 200 images taken along 3.3 seconds), and subtracting that average to the images in that sample. Because lasers 1 and 2 provided with different intensities, separate averaging

and subtraction was made for odd and even images.

3.2.2 Particle Tracking Velocimetry

Different software packages were utilized to track particles and provide their velocities in the images supplied by the high resolution camera. In general, those programs divide the images in smaller parts, the "interrogation areas", in which they try to follow the motion of individual particles. One of them was provided by Dr. Tomomasa Uemura (Uemura and Yamamoto 1993) and works under Microsoft Windows environment. This is one of the most versatile codes for PTV, since it allows to vary practically all parameters and conditions, like grayscale threshold and cluster size, that play a role in a successful processing. It is also highly computationally efficient and fast, and economical in memory requirements. It is based on the identification of similar particle patterns, in which a particle is traced along successive binarized images by means of a binary cross correlation scheme. Particle centroids are spotted using the center of gravity technique.

A home made code, and the oldest ones used in the laboratory, is actually constituted by two Fortran 77 programs working under Unix, the Fspots and Tracking codes. It also uses the center of gravity method to locate the particle centers of gravity (Hassan et al. 1992).

A last code, recently developed by Dr. Hassan's team (Perez Estrada 2004) is the MaskPTV program. It works in Windows environment and utilizes the mask cross correlation technique to calculate a correlation coefficient that is assigned to pixels

whose grayscale is greater than a certain threshold. Then they are grouped together in objects or particles, whose centroids are made out by sub-pixel interpolation or center of gravity methods. The tracking follows basically the same philosophy as the Tracking program.

In any PIV/PTV method in general, the velocity of a particle, which is assumed to follow the fluid, that undergoes a displacement $\Delta\mathbf{x}$ along an interval of time Δt between images is given by (Adrian 1986):

$$\vec{\mathbf{V}} = \lim_{\Delta t \to 0} \frac{\Delta \mathbf{x}}{\Delta t} \tag{3.1}$$

3.2.3 Velocity Field Filtering and Interpolation

Any of the aforementioned codes generates 2D velocity fields that are mostly noisy and have non-uniform random coordinate meshes, so it is imperative to take a last step in conditioning them. This is made in two stages, being the first one, separated itself into two independent processes, just for getting rid of spurious vectors. One process, usually performed in the same PTV program, employs the cross correlation coefficient (CCC) as threshold. Those velocity vectors whose CCC is below a certain pre-established value are disregarded. In general, this step removes 50% of all the vectors. The other process is carried out by a separate program that separates the spatial frame into small interrogation areas and apply basic statistics (average and standard deviation) into each of them. Then this program eliminates those vectors falling outside the average ± a number of standard deviations (usually one or two). In this way, about another 10%

of vectors is purged. Then the instantaneous velocity fields resulting from both processes are combined into one field, which has in average around 1500 vectors / cm^2.

The last step, which gives the velocity fields utilized for this work, is an interpolation aimed at producing regularly spaced vector field. No information is eliminated, but redistributed by applying the inverse distance algorithm in Tecplot, a commercial software package. For this work, all the resulting velocity fields had uniform 50×50-grid-point meshes.

3.3 Main Flow Characteristics

Among the twenty sets, for this study three of single phase and four of two-phase flows (with α = 2.4, 3.4, 4.4, and 4.9 %) were chosen. The most important mean parameters computed for the single and two-phase cases from the velocity fields, pressure, and wall shear stress, are shown in Table 3.1 (for more parameters see Gutierrez Torres 2004). For single phase the value of τ_ω used for all calculations was the one determined from the pressure gradient, equation 2.2. For two-phase the value of τ_ω used was the one determined from the velocity gradient, equation 2.3. The drag reduction is given by:

$$DR = \left(1 - \frac{\tau_\omega}{\tau_{\omega_0}}\right) \times 100 \tag{3.2}$$

Table 3.1 shows the increment in drag reduction that accompanies the injection of microbubbles into a turbulent boundary layer. In the following section effects on

vortical structures will be analyzed.

α	$\mathrm{Re}_h = \frac{U_b h}{\nu}$	$\tau_\omega = -h\frac{dP}{dx}$ [a] [N/m^2]	$\tau_\omega = \mu \left.\frac{dU}{dy}\right\|_{y=0}$ [N/m^2]	$\tau_{\omega\ \text{Optical Sensor}}$ [a] [N/m^2]	$u_\tau = \left(\frac{\tau_\omega}{\rho}\right)^{1/2}$ [b] [mm/s]	$\mathrm{Re}_\tau = \frac{u_\tau h}{\nu}$	DR %
0	5128	0.160	0.139	0.150	12.6	371	0
2.4	5128	-	0.117	0.135	10.8	317	12.9
3.4	5128	-	0.112	0.135	10.6	311	16.1
4.4	5128	-	0.094	0.135	9.7	284	29.8
4.9	5128	-	0.083	0.135	9.1	267	38.2

Table 3.1. Average flow parameters for single and two-phase flows (water, 20 °C)

[a] From Dominguez Ontiveros 2004.
[b] From Gutierrez Torres 2004.

4 VORTEX VISUALIZATION AND IDENTIFICATION

There is still a strong debate on how to define a vortex, mainly in turbulence and complex flows in general. As a result, the many schemes for the identification of a vortex that have been suggested have also proven to have a limited effectiveness (Jeong and Hussain 1995; Zhou et al 1999). In general, they follow different paradigms that focus on specific flow field parameters or characteristics that are meant to be strongly influenced by the presence of a vortex.

4.1 Vorticity

Vorticity has historically been related to rotational flows, especially turbulent flows. It has also been the parameter most widely associated to the presence and features of vortical structures and eddies, either as a component of the vorticity vector (Jiménez et al. 1988; Antonia et al. 1988; Brooke and Hanratty 1993; Hanratty and Papavassiliou 1997; Klewicki 1997), or as vortex lines or tubes (Moin et al. 1986; Kim and Moin 1986). It also proved useful in showing many aspects of shear stress distribution in the near-wall region. For example, Kim (2003) used isovorticity maps along wall-normal-spanwise directions to show the weakening of streamwise vortices by means of a turbulent boundary layer control system. Besides, Gutierrez Torres (2004) demonstrated how the injection of microbubbles into a turbulent boundary layer leads to the diminution in vortex stretching, regarded as a source of high vorticity levels.

For this work, because of the two-dimensionality of the velocity field, only the

spanwise component of the vorticity vector, that is ω_z, has been calculated. Following equation 1.9, and the nomenclature given at the beginning of section 3:

$$\omega_z = \frac{\partial v}{\partial x} - \frac{\partial u}{\partial y} \tag{4.1}$$

In the 50×50 control volumes that comprise the given velocity fields, this z-vorticity is approximated by second order finite difference schemes, central difference for inner grid points, and forward or backward differences for boundary points, assuming uniform meshes. Following Fig. 4.1, these differences are given by (see Chung 2002):

Central difference:
$$\left(\frac{\partial u}{\partial x}\right)_i = \frac{u_{i+1} - u_{i-1}}{2\Delta x} \tag{4.2}$$

Backward and forward differences:
$$\left(\frac{\partial u}{\partial x}\right)_i = \frac{\mp 3u_i \pm 4u_{i\pm 1} \mp u_{i\pm 2}}{2\Delta x} \tag{4.3}$$

The sign convention is: upper sign for forward difference, and lower for backward. This equation is applicable when differentiating respect to *y*, by changing sub-index *i* by *j*. The same for the *v* component of the velocity.

A special observation must be made at this point regarding the boundary of the control volume lying on the wall. Because of noise and other measurement constraints, the closest to the wall it was possible to track particles was around 1½ Δy. However, the non-slip condition was assumed, so both velocity components were taken equal to zero on the wall and corresponding grid points were added to the velocity fields.

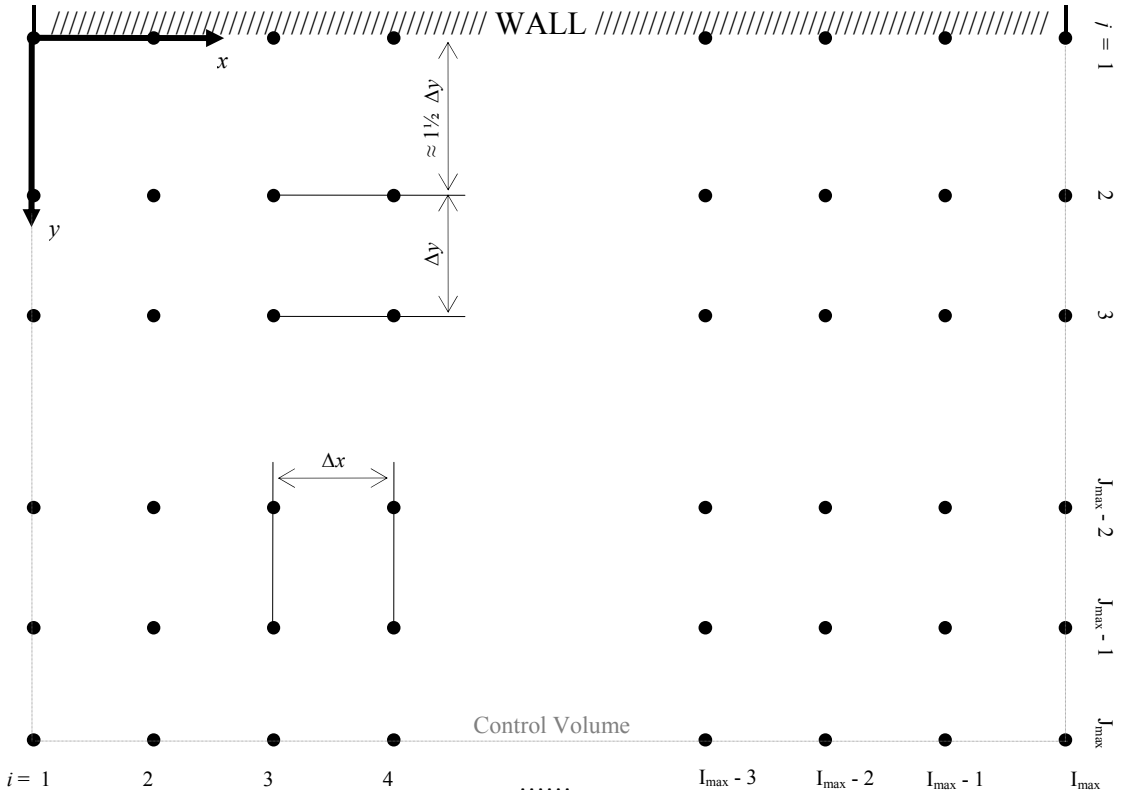

Fig. 4.1. Control volume mesh

Results of instantaneous vorticity fields calculated for single phase and for void fractions α = 2.4 to α = 4.4 are shown in Fig. 4.2 and Fig. 4.3. It is noticeable the gradual diminution in vorticity levels, especially close to the wall, from single phase to two phase, and in this case, from α = 2.4 to α = 4.4. This shows in the most unambiguous and direct way the effects of microbubble injection on shear stress production, which is to reduce it.

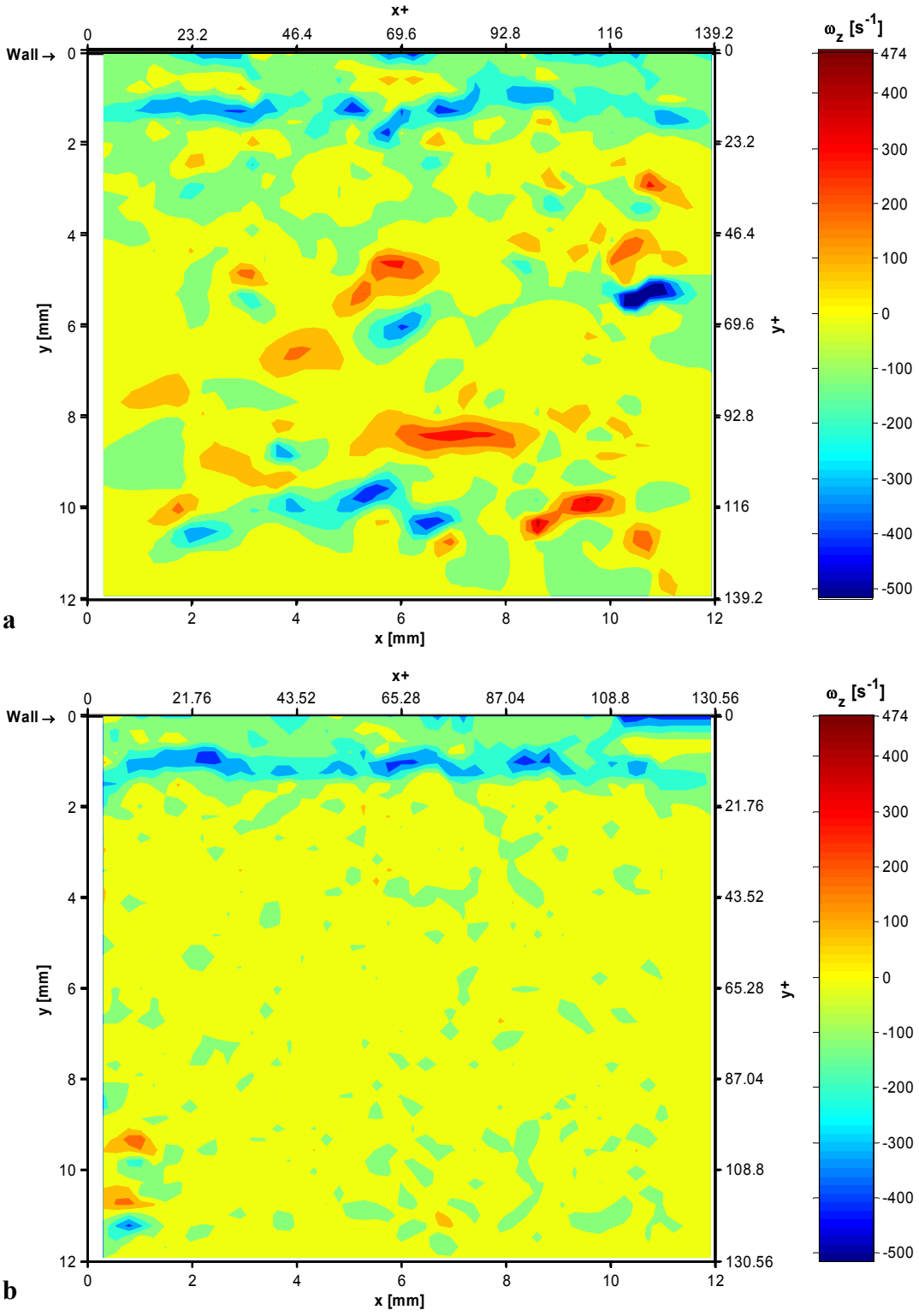

Fig. 4.2. Instantaneous vorticity field **a** single phase flow; **b** $\alpha = 2.4\%$, DR = 12.9%

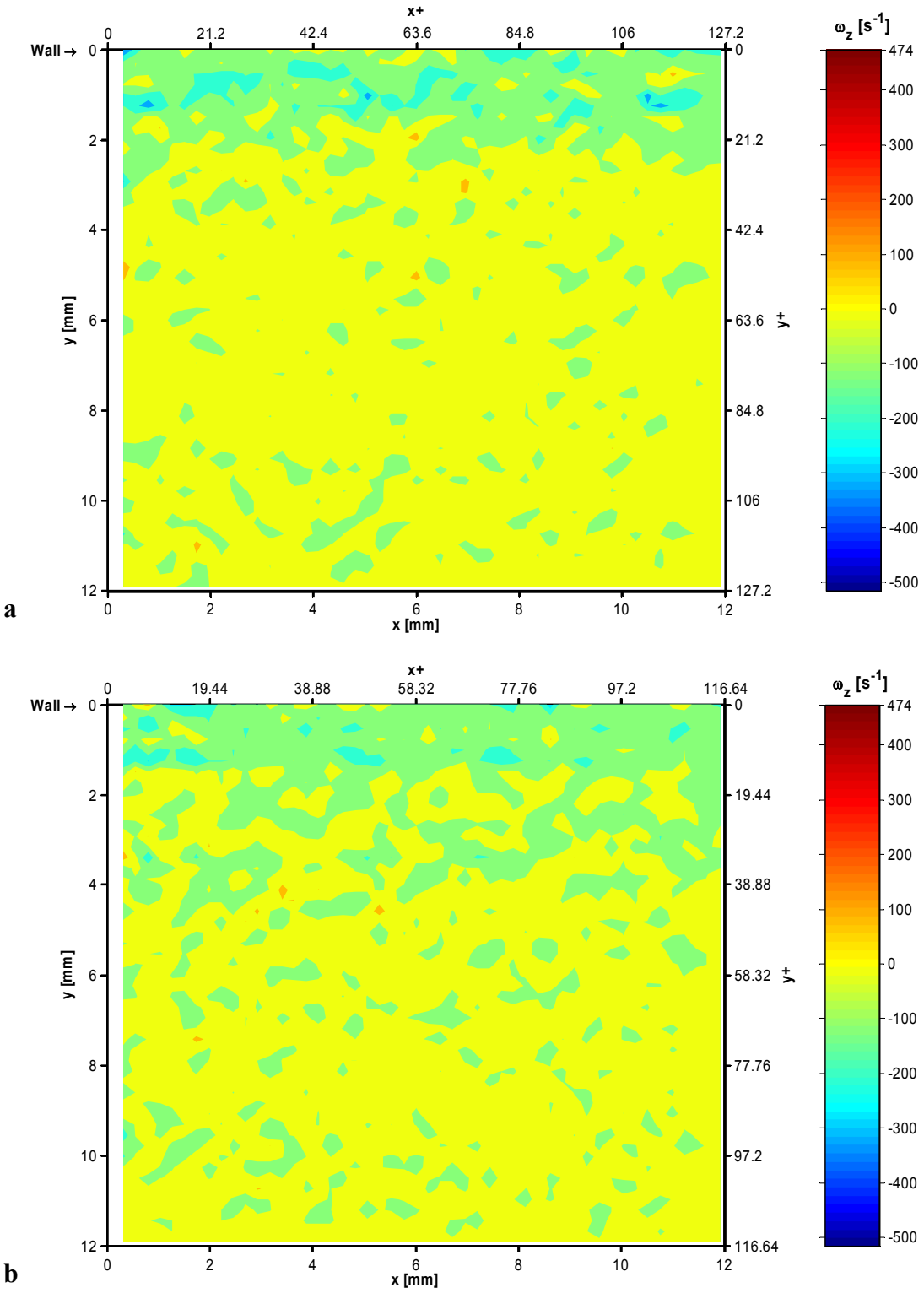

Fig. 4.3. Instantaneous vorticity field **a** α = 3.4%, DR = 16.1 %; **b** α = 4.4% , DR = 29.8 %

The trend of gradual diminution in vorticity levels is continued in Fig. 4.4, which presents the instantaneous vorticity field for α = 4.9.

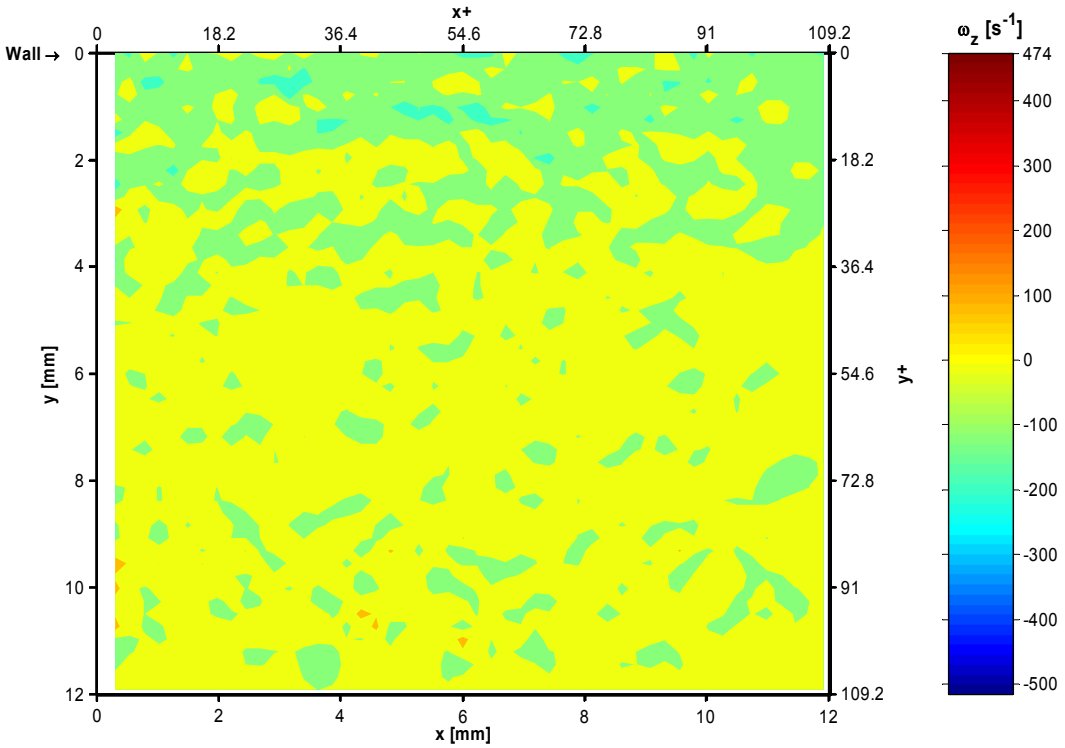

Fig. 4.4. Instantaneous vorticity field for α = 4.9%, DR = 38.2 %

The vorticity fields were averaged along the time for each data set, and plotted, for single phase and for void fractions α = 2.4 to α = 4.4, in Fig. 4.5 and Fig. 4.6. Again, the same trend is shown as with the instantaneous vorticity fields, with emphasis close to the wall, which is actually where most shear stress is produced.

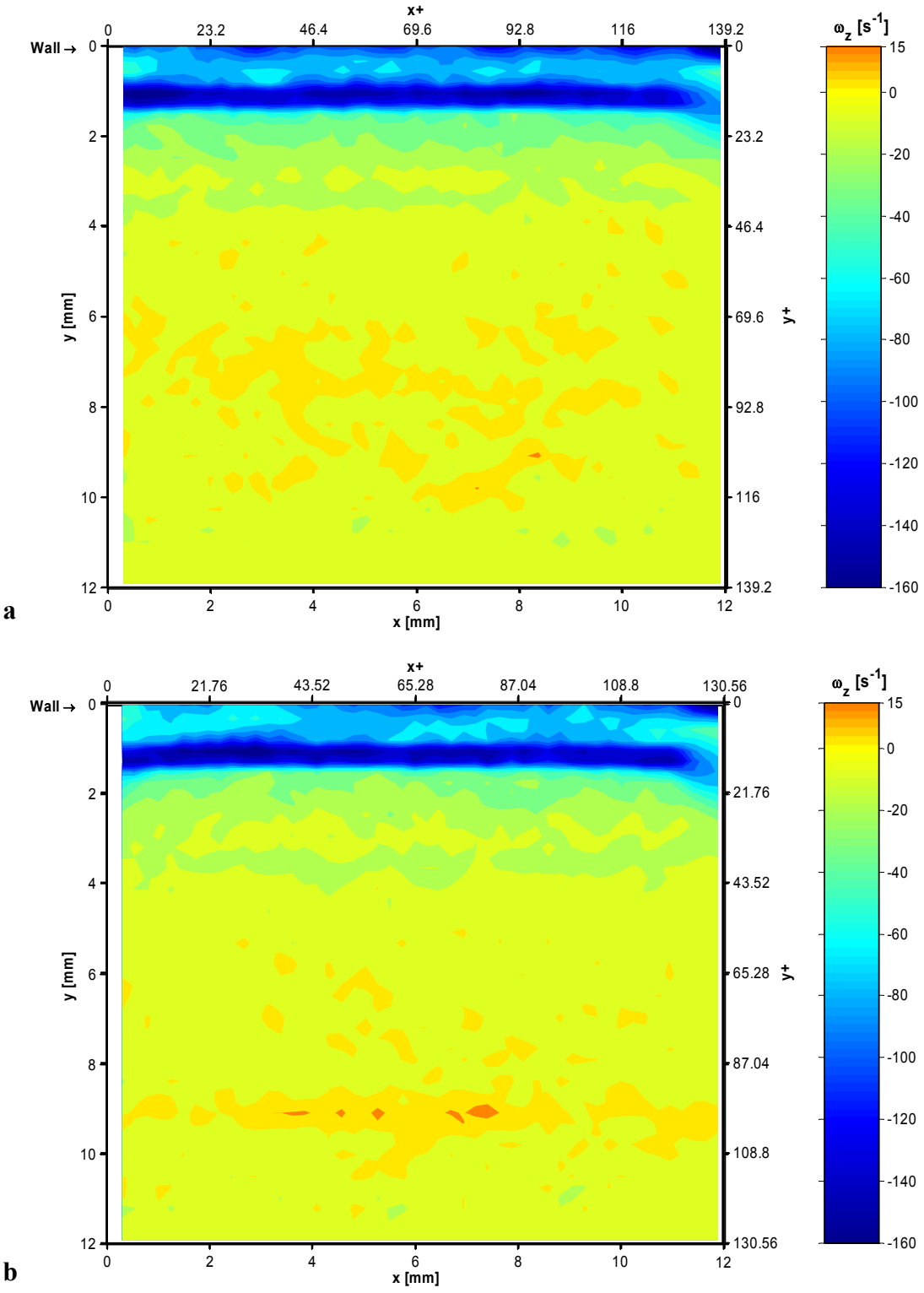

Fig. 4.5. Time averaged vorticity field for **a** single phase flow; **b** $\alpha = 2.4\%$, DR = 12.9%

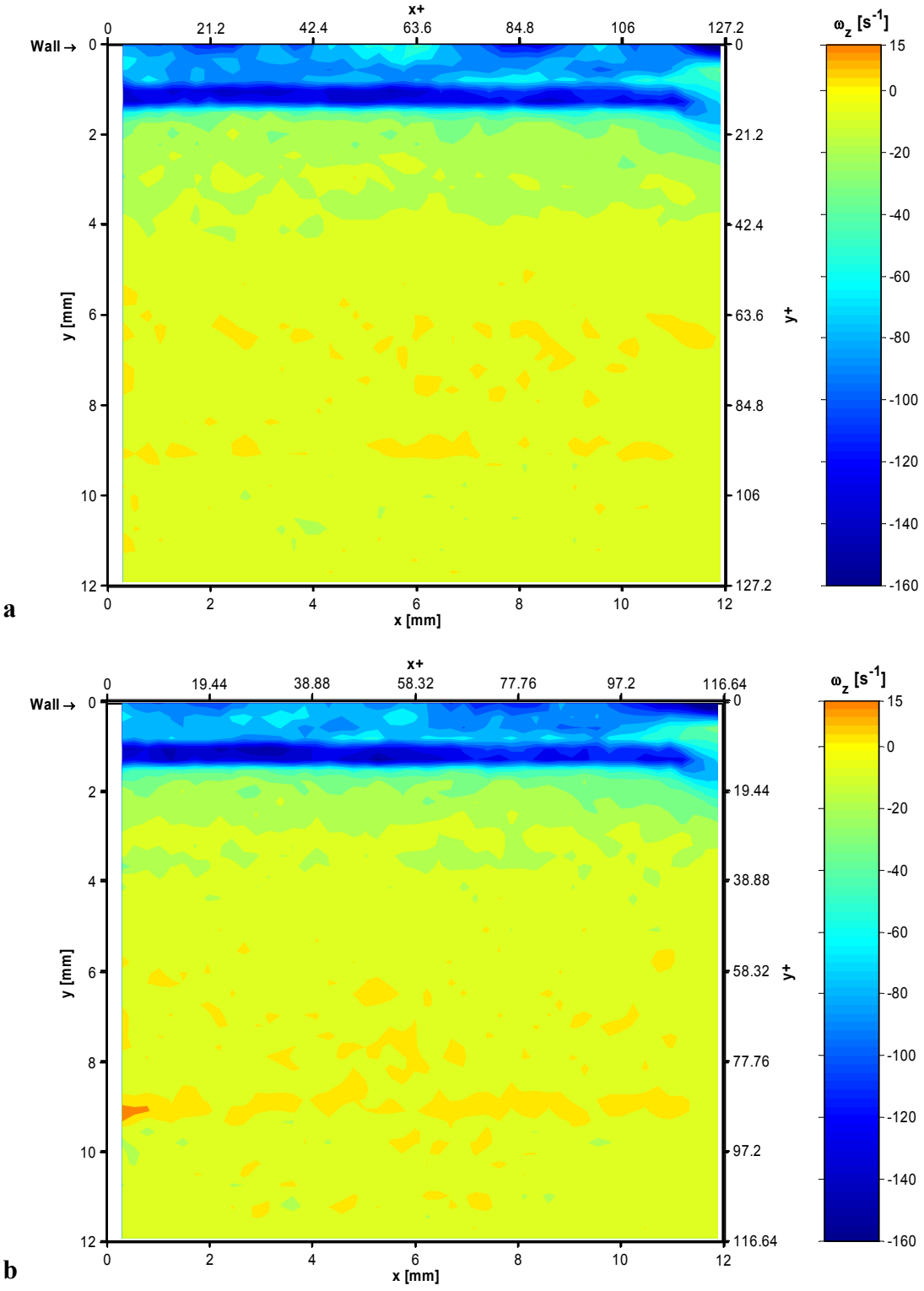

Fig. 4.6. Time averaged vorticity field for **a** α = 3.4%, DR = 29.8 %; **b** α = 4.4%, DR = 16.1 %

The trend of gradual diminution in vorticity levels is continued in Fig. 4.7, which presents the time averaged vorticity field for α = 4.9.

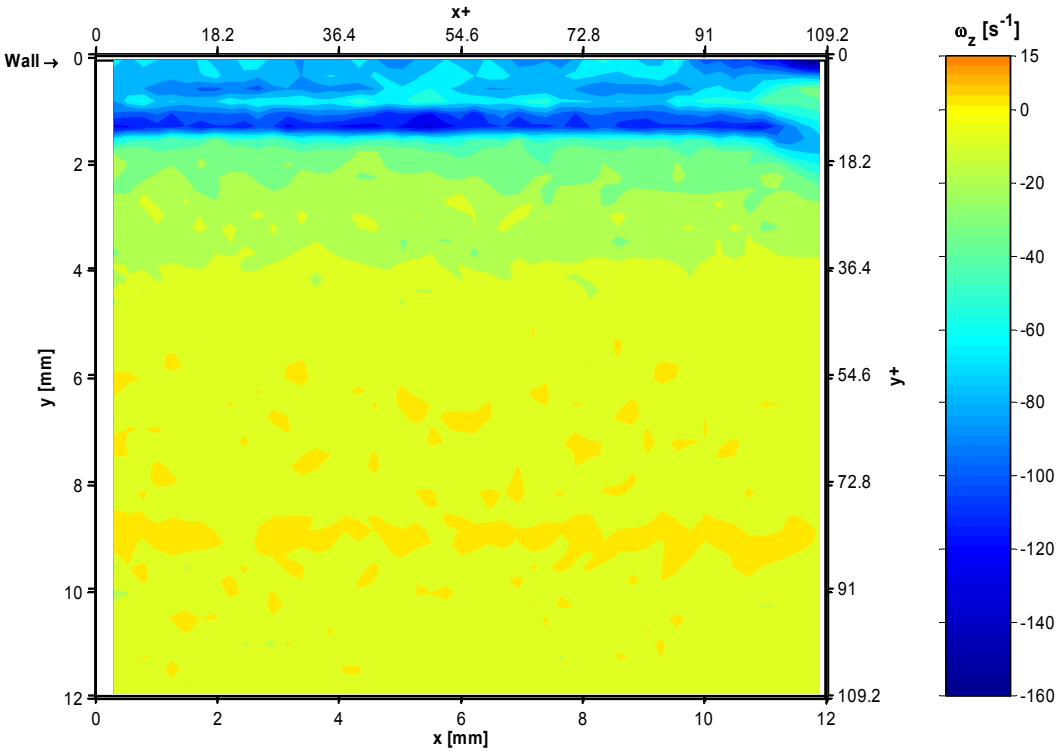

Fig. 4.7. Time averaged vorticity field for α = 4.9%, DR = 38.2 %

4.2 Galilean Decomposition

From a point of view of vortex detection, vorticity alone is scarcely effective, especially if the vortex surroundings have the same, or higher shear stress. This is why vorticity maps are usually presented along with other methods, like Galilean transformation, or Reynolds decomposition. The idea behind the use of closed streamlines or pathlines to recognize a vortex is that the flow shows more or less circular or spiral motion patterns concentric to the vortex core, at least when its core stays fixed

in the chosen reference frame (Lugt 1979; Robinson et al. 1988). This last condition constitutes the mean weakness of this method, since it requires a previous knowledge of the core location and velocity, so it must always be compared against less frame dependant schemes. However, different field decompositions, which can reveal the vortex cores by exposing the diverse scales present in the flow field, are still being applied with very good results (Adrian et al. 2000; Wu 2004; Christensen et al. 2004; Hassan et al. 2004; Gutierrez Torres 2004).

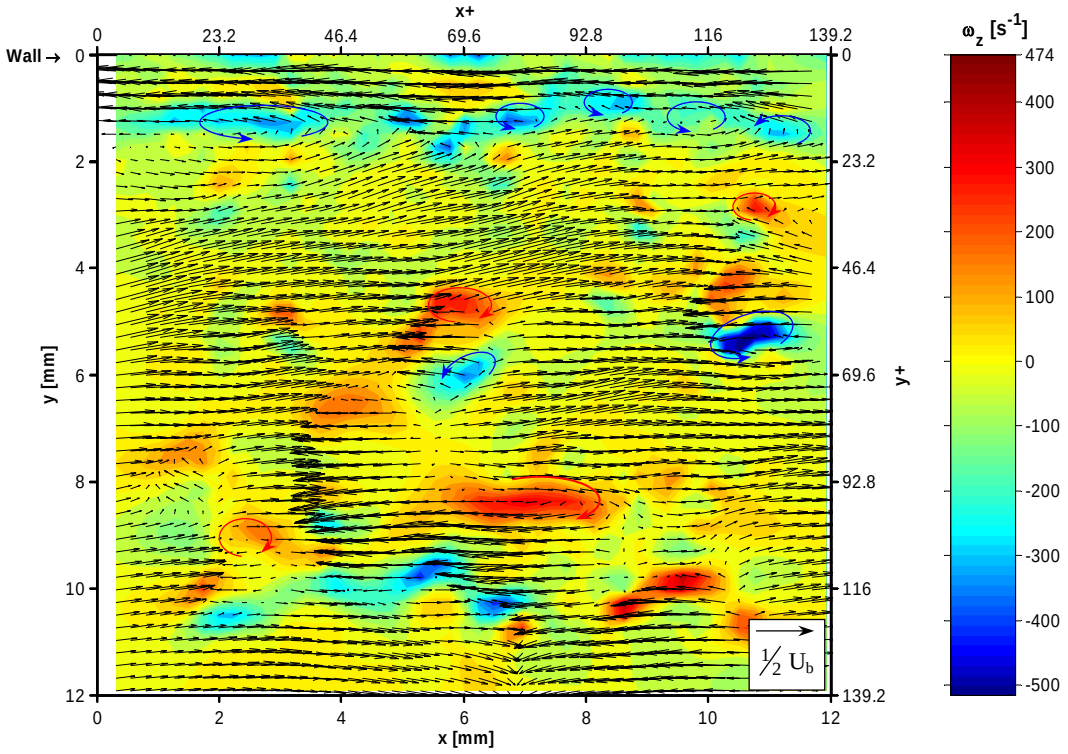

Fig. 4.8. Instantaneous vorticity and Galilean decomposed velocity field, single phase flow, U_{adv} = 0.77 U_b; red arrow (+) vortex, blue arrow (-) vortex

In Galilean decomposition, a constant advection velocity U_{adv} is subtracted from the whole velocity field, revealing in this way the vortex cores traveling at that velocity.

In general, it is calculated as a fraction of a characteristic velocity in the flow, like the centerline, bulk, or a space average velocity. For this work, the bulk velocity U_b was chosen, so $U_{adv} = f \cdot U_b$, where f is generally between 0.5 and 1.0.

In figures 4.8 through 4.10 instantaneous velocity and vorticity fields in single phase flow are shown. The velocity was subtracted different fractions of U_b to reveal counter-clockwise vortices (in red), and clockwise vortices (in blue). It is noticeable that vortices farther from the wall have higher advection velocities. Also, positive vortices are more easily found farther from the wall than negative ones.

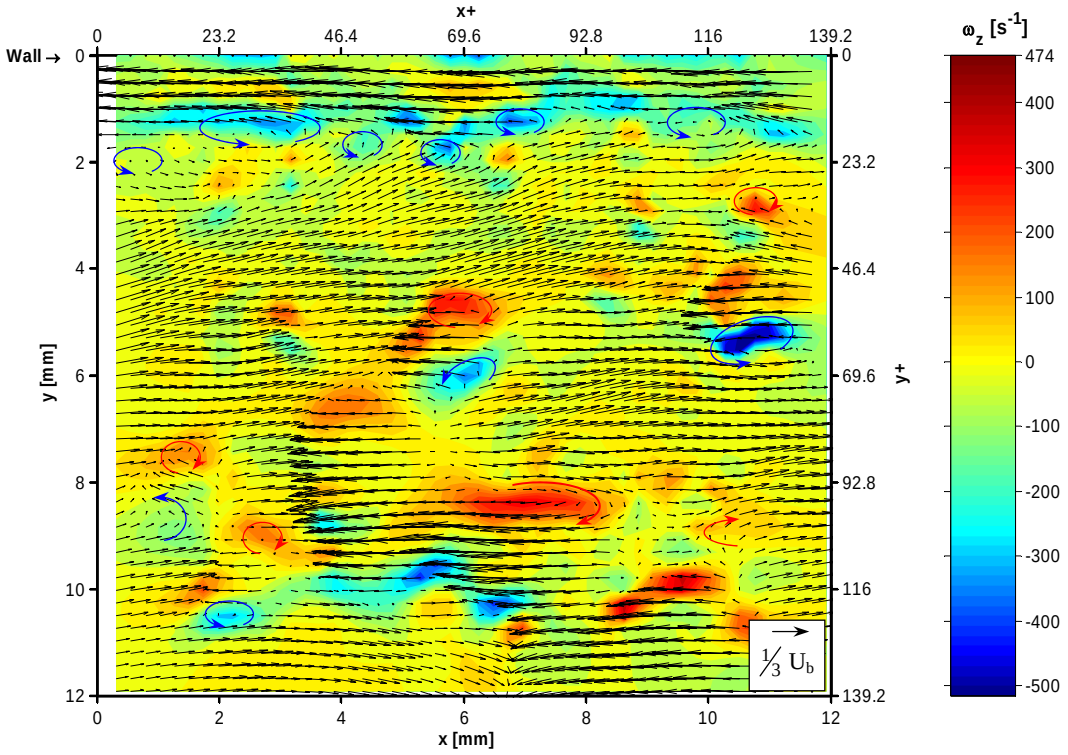

Fig. 4.9. Instantaneous vorticity and Galilean decomposed velocity field, single phase flow, $U_{adv} = 0.83\ U_b$; red arrow (+) vortex, blue arrow (-) vortex

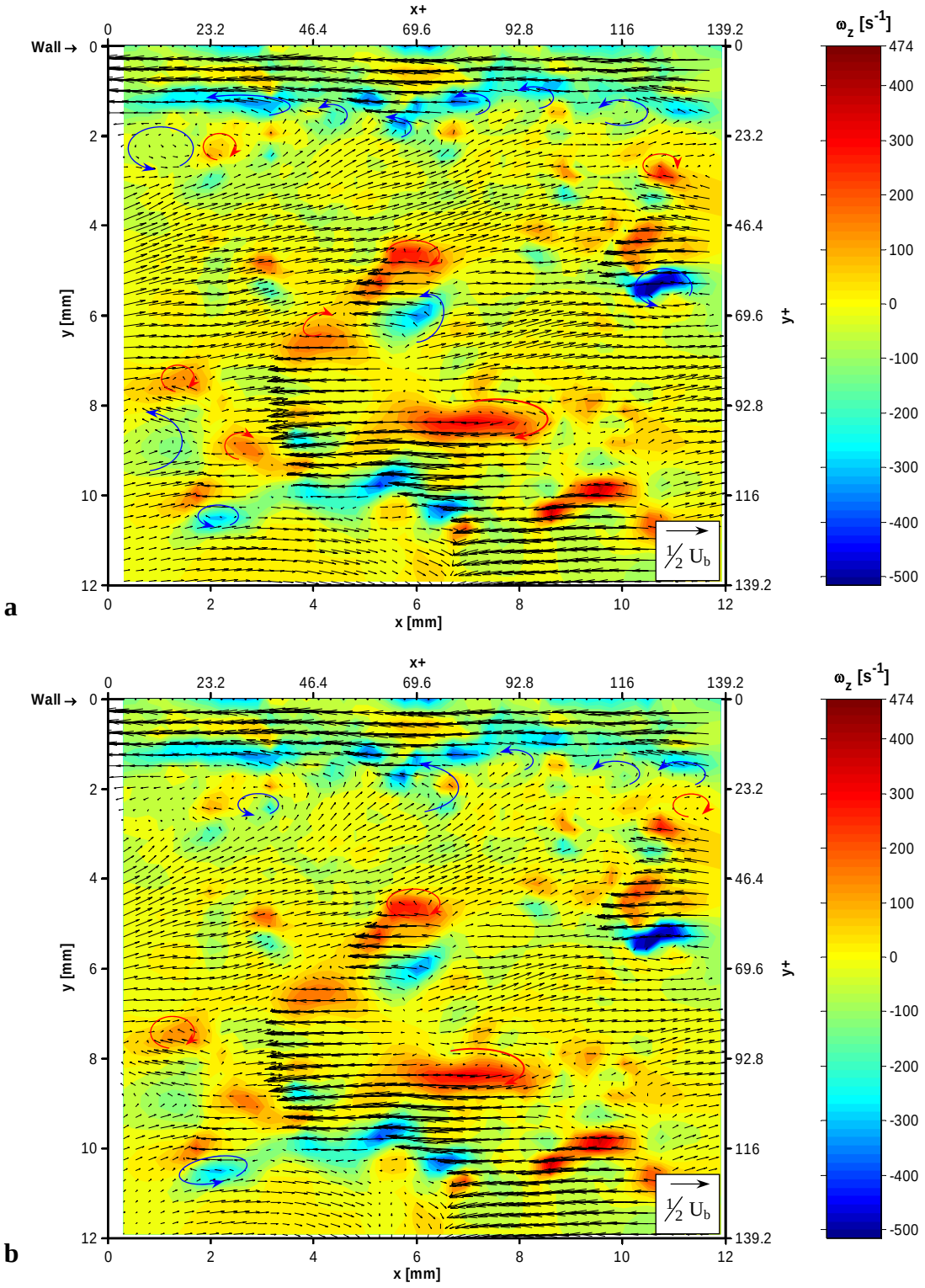

Fig. 4.10. Instantaneous vorticity and Galilean decomposed velocity field, single phase flow, **a** U_{adv} = 0.88 U_b; **b** U_{adv} = 0.95 U_b; red arrow (+) vortex, blue arrow (-) vortex

Galilean decomposition was also applied to microbubble-injected flow with the maximum void fraction $\alpha = 4.9$ and the results are presented in Fig. 4.11. The same observations regarding vortices are applicable.

4.3 Reynolds Decomposition

In a velocity field, the component with the largest scale in either time or some spatial subset can be estimated by averaging the velocity along those respective dimensions; then, by subtracting that average from the original velocity field, one would reveal the smaller scales (Adrian et al. 2000). In the case of channel flows, vortical structures have scales that are smaller than those of the mean flow field, so this method, the Reynolds decomposition into an average component and a fluctuation, is basically another method of identifying the vortex core advection velocity. The average component can be calculated by any of the integral methods given in section 1, although most people use time averaging. As in Galilean decomposition, it can be multiplied by a factor before being subtracted from the velocity field, so the decomposition will be:

$$\mathsf{u} = f \cdot \overline{\mathsf{U}} + \mathsf{u}' \tag{4.4}$$

For this work, the time average $\bar{\mathbf{U}} = \bar{\mathbf{U}}(x,y)$ defined by equation 1.11 was used, and the results for both single phase and the maximum void fraction $\alpha = 4.9$ are shown in Fig. 4.12.

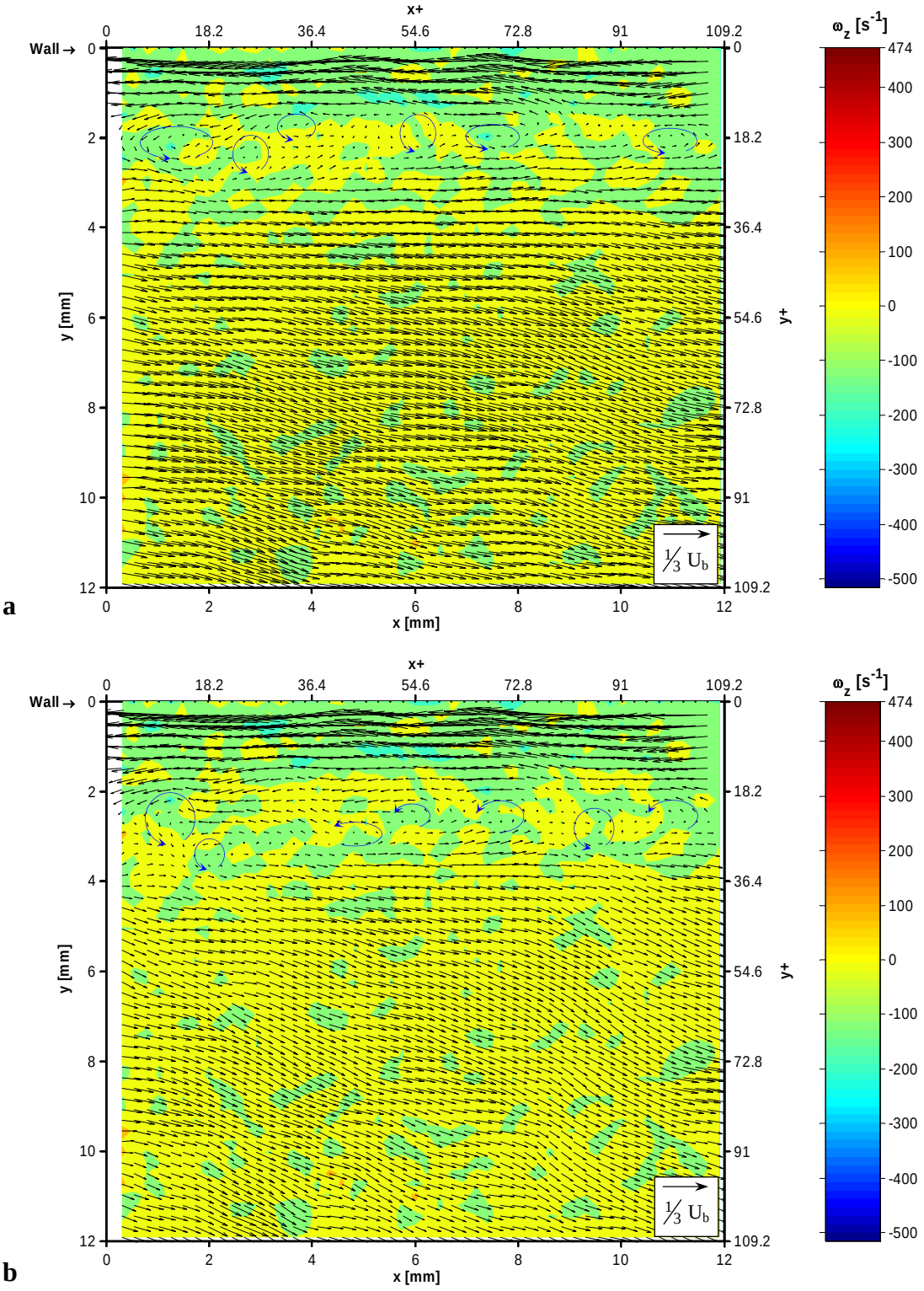

Fig. 4.11. Instantaneous vorticity and Galilean decomposed velocity field, α = 4.9%, **a** U_{adv} = 0.56 U_b; **b** U_{adv} = 0.65 U_b; red arrow (+) vortex, blue arrow (-) vortex

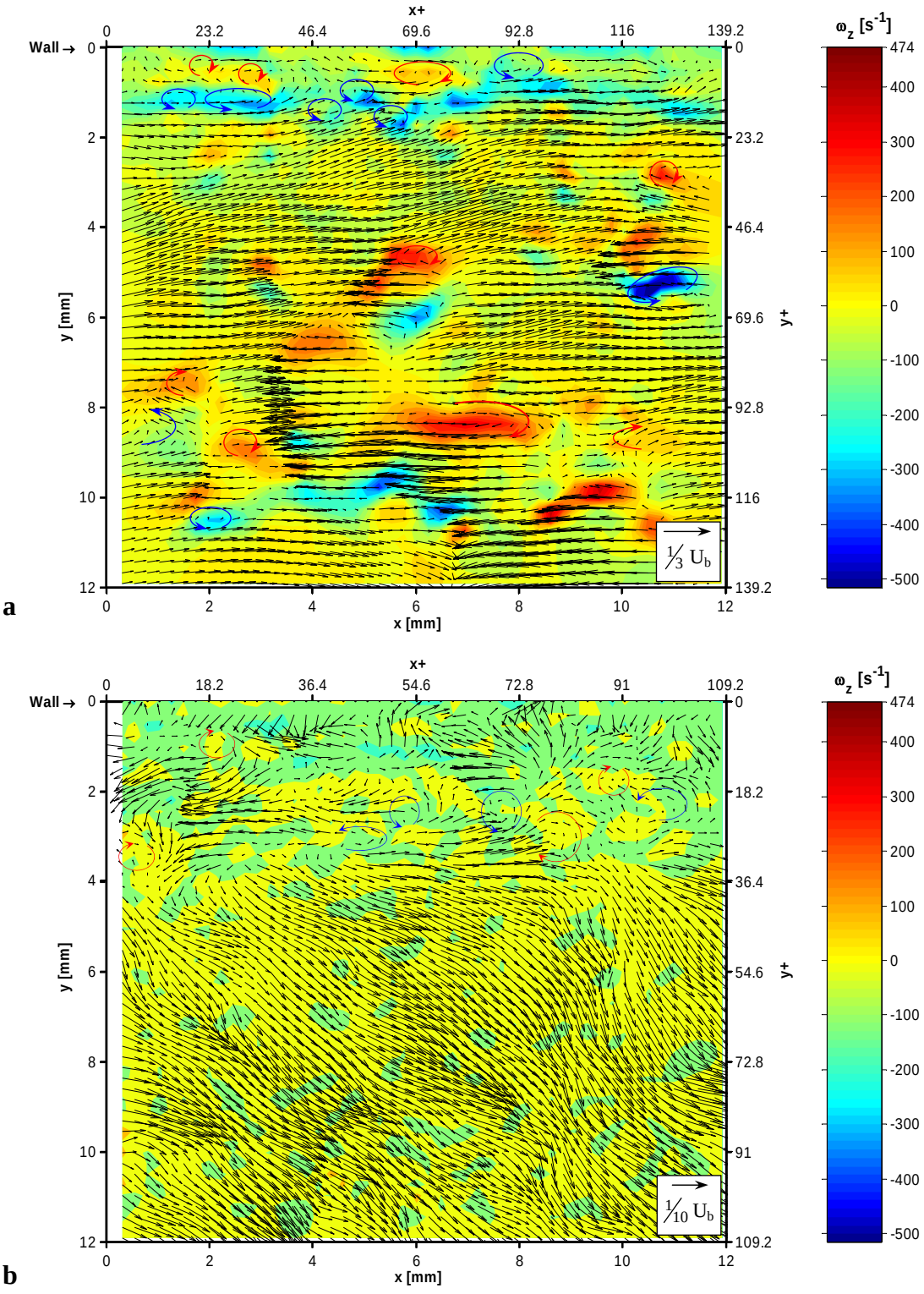

Fig. 4.12. Instantaneous vorticity and Reynolds decomposed velocity field, **a** single phase, f = 0.90; **b** α = 4.9%, f = 0.82; red arrow (+) vortex, blue arrow (-) vortex

Reynolds decomposition, when compared to Galilean decomposition, reveals vortices closer to the wall, besides most of those identified with that technique. Also, vortices at a wider range of y-positions are exposed in both single and two-phase flows.

4.4 Swirling Strength

As it was said, the main drawback of the decompositions is that they are sensible to any Galilean coordinate transformation of the form (see Haller 2005):

$$\mathbf{x}_2 = \mathbf{A} \cdot \mathbf{x}_1 + v \cdot t \tag{4.5}$$

Where v is a constant velocity and **A** is a proper orthogonal tensor that represents the rotation of fluid particles. The term $v \cdot t$ makes vorticity also problematic, so a Galilean-invariant vortex criterion becomes a must. It is desirable a scalar field whose value, preferably limited to a fixed range, is directly associated to the presence of circle-like rotational patterns in the flow, and does not change if the flow field coordinate system undergoes arbitrary translations or rotations respect to the observer's frame. Early attempts to deal with this issue were based on the three invariants *P*, *Q*, and *R*, of the velocity gradient tensor $\nabla \boldsymbol{V}$, whose symmetric and antisymmetric components, given by equations 1.7 and 1.8, respectively, are fundamental parts in all Galilean-invariant vortex criteria proposed so far. Those early criteria, led by the *Q*-criterion (Hunt et al. 1988) and the Δ-criterion (Chong et al. 1990), relied upon the natural conception that a vortex core is a zone in the flow field where the rotation tensor **Ω**, embodied by the vorticity magnitude, prevails over the strain rate tensor **D**, related to the shear strain.

Chong et al. (1990) considered a coordinate system that moves without rotate solidary to the fluid particle. The flow at the origin of that coordinate system constitutes a critical point, i.e. its velocity magnitude is zero. They suggested that the velocity gradient tensor has complex eigenvalues at a vortex core, so the discriminant of the characteristic equation $\lambda^3 - P\lambda^2 + Q\lambda - R = 0$ is positive:

$$\Delta = \left(\frac{1}{3}Q\right)^3 - \left(\frac{1}{2}R\right)^2 \tag{4.6}$$

Where:

$$\mathrm{P} = \frac{\partial V_i}{\partial x_i} \qquad \left(\text{zero for incompressible flow}\right) \tag{4.7}$$

$$\mathrm{Q} = \frac{1}{2}\left[P^2 - tr\left(\left(\nabla V\right)^2\right)\right] \tag{4.8}$$

$$\mathrm{R} = -\det\left(\nabla V\right) \tag{4.9}$$

Following this idea, Zhou et al. (1996) used the imaginary part of the complex eigenvalues of the velocity gradient tensor to identify vortices. This scalar, called swirling strength (Zhou et al. 1999), can also be defined for two-dimensional flow fields (see Adrian et al. 2000) as:

$$\lambda_{\mathrm{ci}} = \mathrm{Im}\left[eig\left(\nabla V\right)\right] = \frac{1}{2}\mathrm{Im}\left\{\sqrt{\left(\frac{\partial u}{\partial x} - \frac{\partial v}{\partial y}\right)^2 + 4 \cdot \frac{\partial u}{\partial y} \cdot \frac{\partial v}{\partial x}}\right\} \tag{4.10}$$

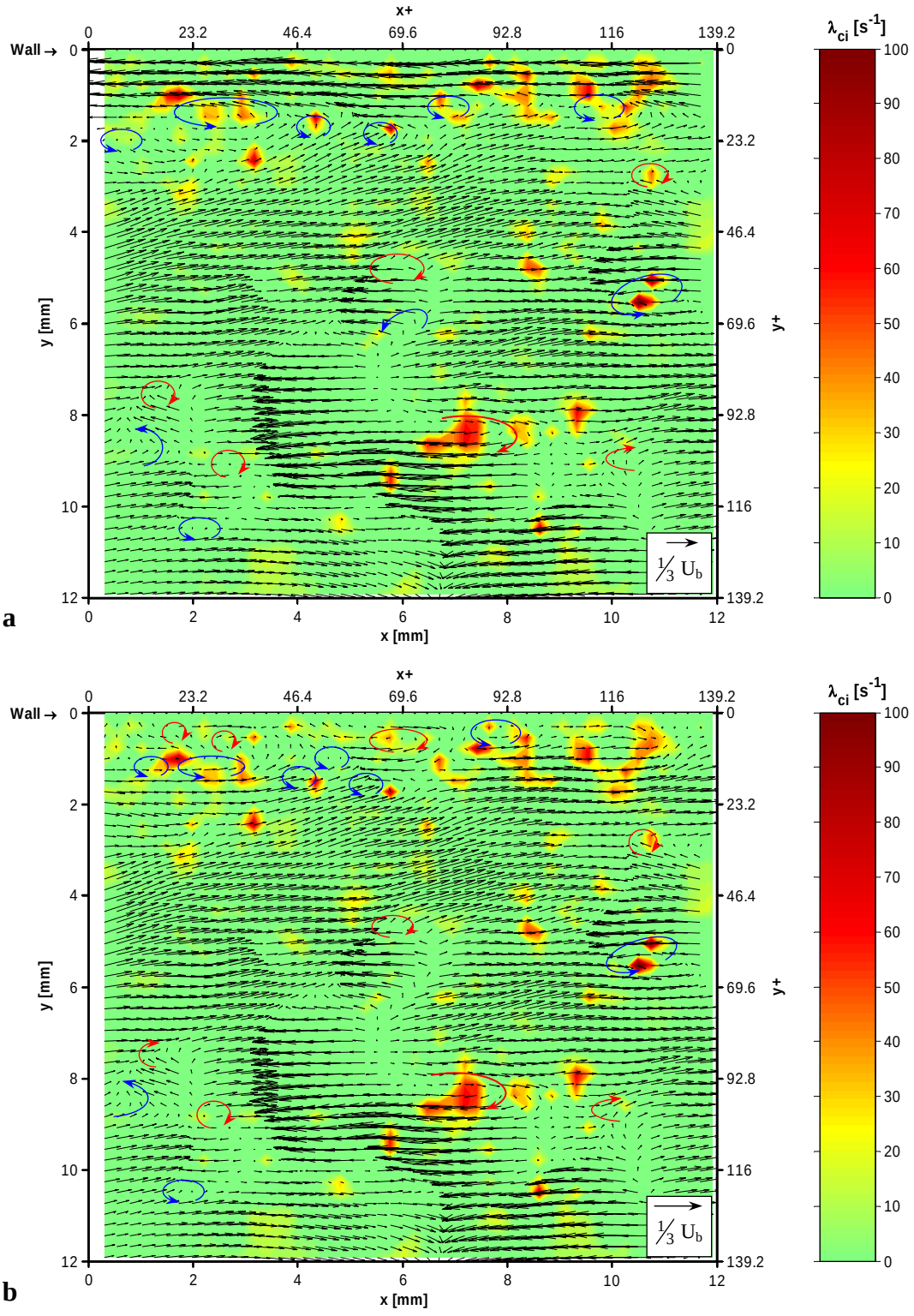

Fig. 4.13. Instantaneous λ_{ci} and velocity field, single phase, decomposed with **a** Galilean $U_{adv} = 0.83\ U_b$; **b** Reynolds $f = 0.90$; red arrow (+) vortex, blue arrow (-) vortex

This λ_{ci} was calculated with the same finite difference schemes utilized for the vorticity for single and two-phase at the same instants as in figures 4.8 to 4.11, and is presented in figures 4.13 and 4.14. Comparing these figures with those for vorticity, it is noticeable that, although some of the ω_z and λ_{ci} maxima match in many places, the latter demarcates much better the vortex cores, regardless of the background shear stress, by presenting well defined peaks and less noisier valleys. Also, most patterns marked on the vector fields enclose, or are in vicinity to λ_{ci} peaks. However, the λ_{ci} criterion cannot provide the vortex sense of rotation, basically because any vortex core has a pair of conjugate complex eigenvalues not linked to that sense.

4.5 Modified Swirling Strength

By multiplying the swirling strength with the sign of vorticity, Christensen and Wu (2004) proposed a way to combine in a unique parameter the advantages of both swirling strength and vorticity. This modified swirling strength was already defined by equation 1.29 and a more detailed definition is:

$$\Lambda_{ci}(x,y) = \lambda_{ci}(x,y) \cdot \frac{\boldsymbol{\omega}_z(x,y)}{\left\|\boldsymbol{\omega}_z(x,y)\right\|} \tag{4.11}$$

Here the fraction that multiplies λ_{ci} represents the sign of ω_z.

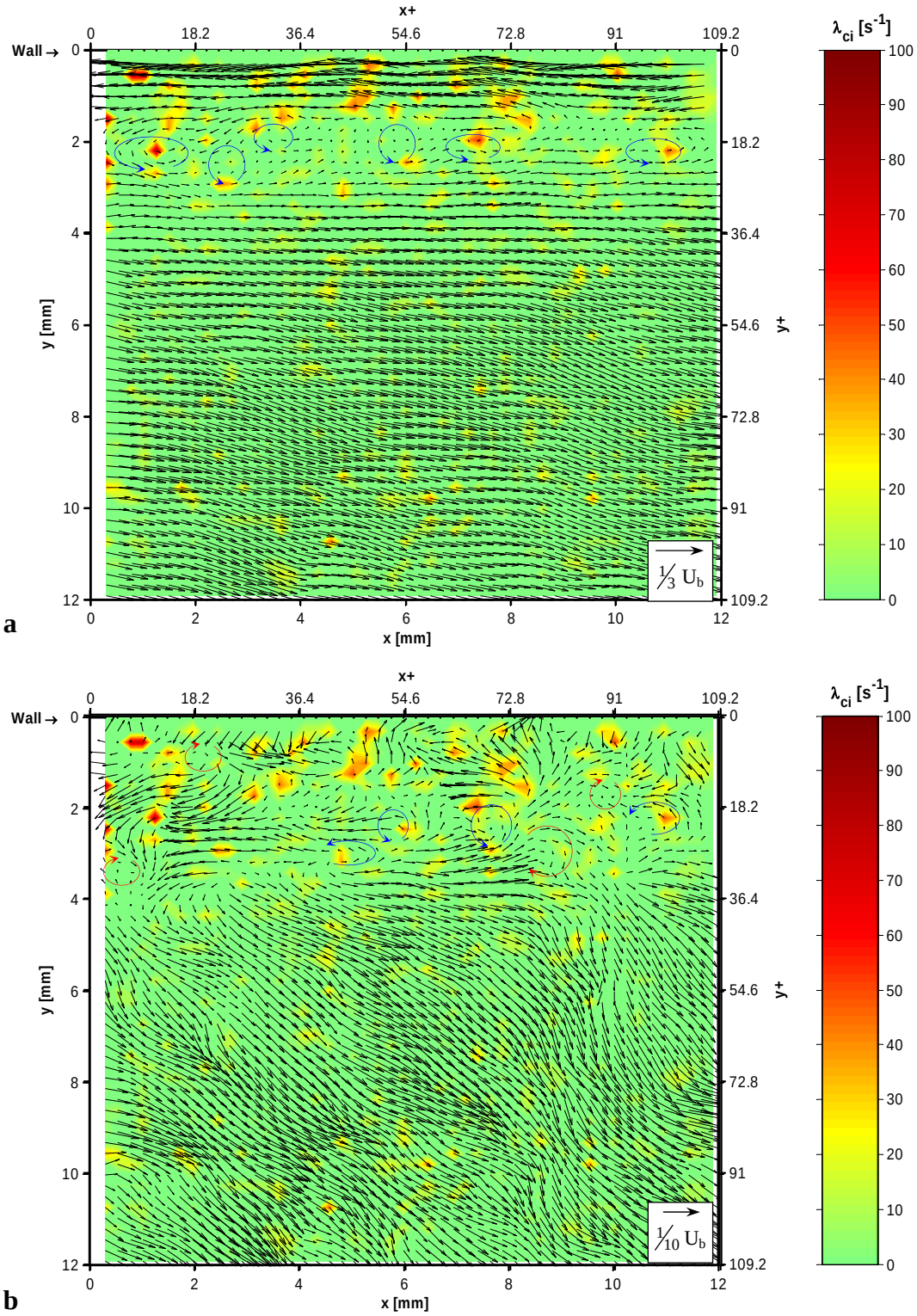

Fig. 4.14. Instantaneous λ_{ci} and velocity field, α = 4.9%, decomposed with **a** Galilean U_{adv} = 0.56 U_b; **b** Reynolds f = 0.82; red arrow (+) vortex, blue arrow (-) vortex

The modified swirling strength was calculated for a single phase flow and compared to Galilean transformation with 80 % of the centerline velocity (U_{cl} = 250 mm/s) removed from the flow field, and shown in Fig. 4.15a.

The effectiveness of the modified swirling strength method is remarkable, especially in marking the larger vortices, or those with a higher swirling strength. It is thus a good idea to restrict the identification process by setting a minimum magnitude of Λ_{ci} to be satisfied. This is accomplished with the root-mean-square (RMS) of the modified swirling strength, calculated as a function of the wall-normal position:

$$RMS_{\Lambda_{ci}}\left(y_j\right)=\sqrt{\sum_{i=1}^{I_{max}}\left[\Lambda_{ci}\left(x_i,y_j\right)\right]^2} \tag{4.12}$$

This filter was calculated and applied separately to positive and negative vortices (because of their different Λ_{ci} magnitudes), and shown in Fig. 4.15b.

The reason for calculating the RMS separately for positive and negative vortices can be realized from Fig. 4.16, where a typical $RMS_{\Lambda_{ci}}$ is plotted versus the y-position. By using the same RMS (the one in blue), too many positive vortices would be discarded close to the wall. In addition, this threshold is almost twice as much as the ones for positive and negative vortices. It can be seen that, regardless of the wall-normal position, major peaks are pretty well outlined.

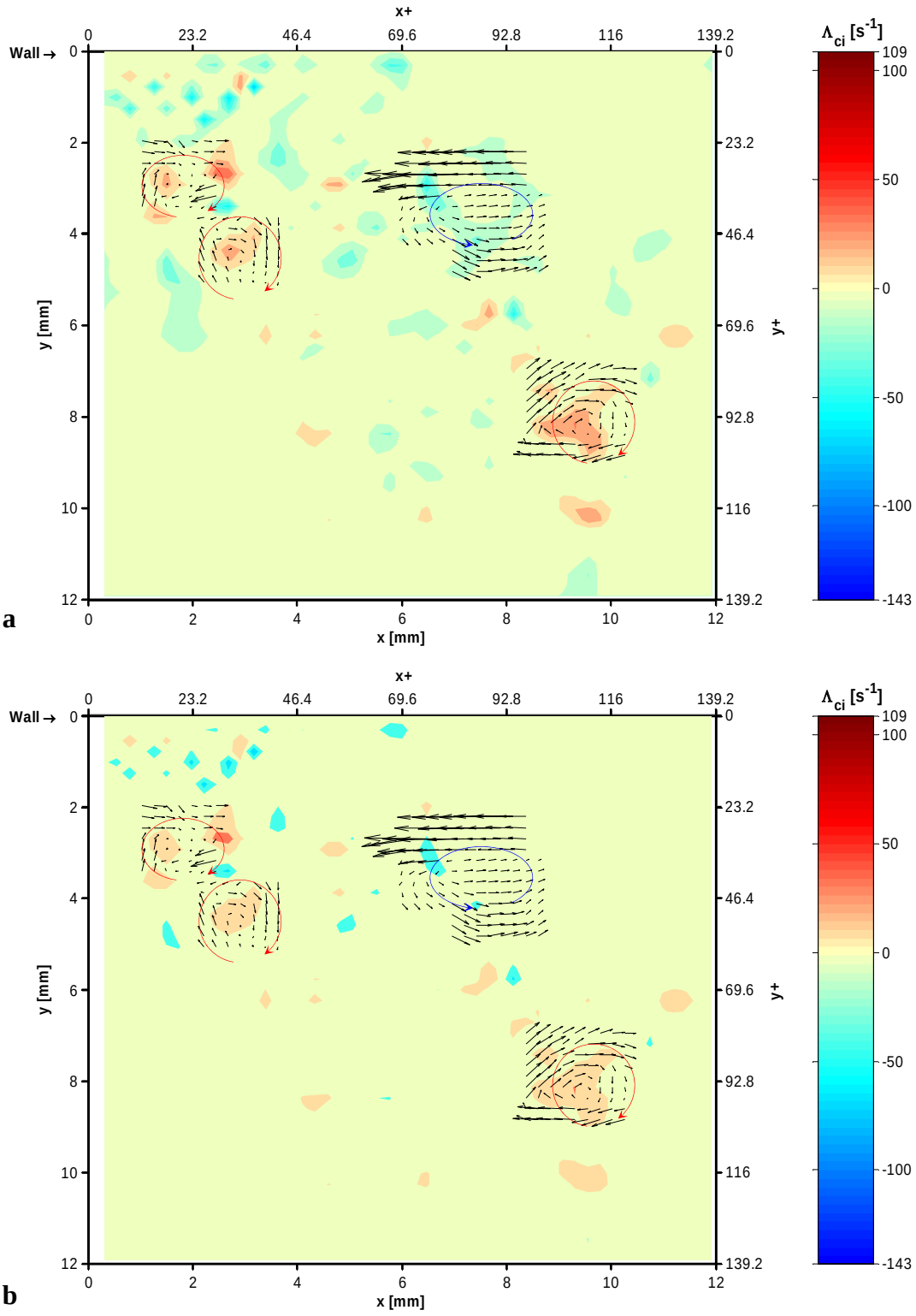

Fig. 4.15. Instantaneous Λ_{ci} and Galilean decomposed velocity field, single phase, U_{adv} = 0.80 U_{cl} **a** unfiltered; **b** filtered with RMS; red arrow (+) vortex, blue arrow (-) vortex

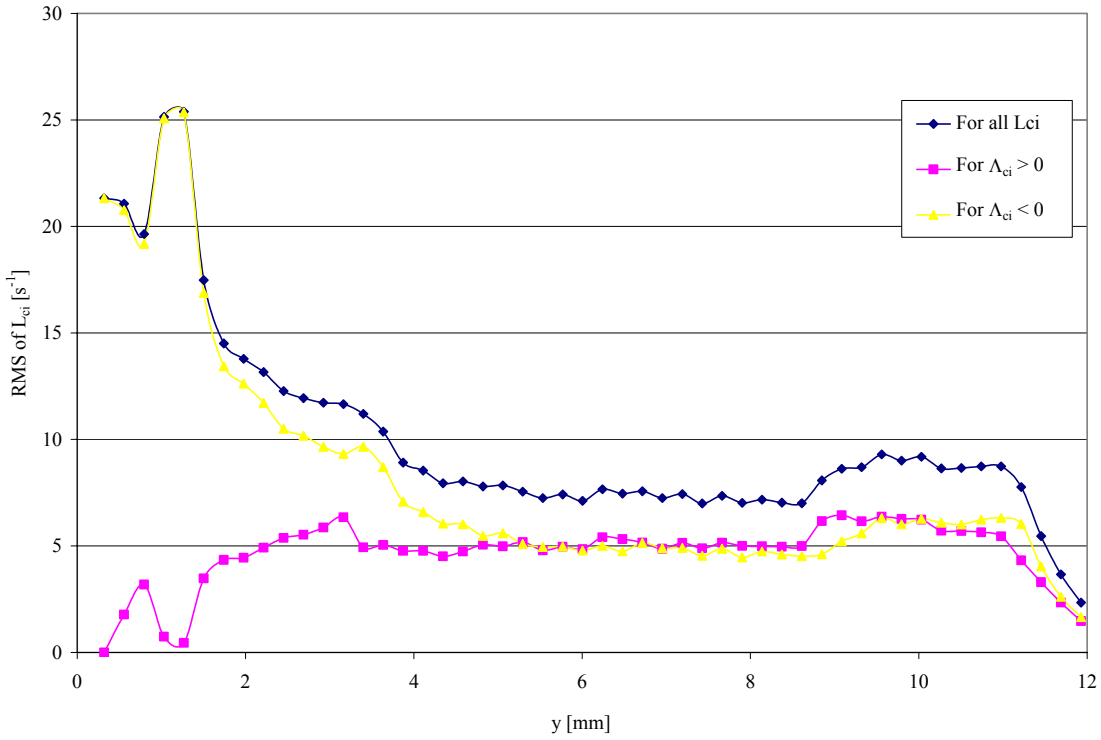

Fig. 4.16. Typical time averaged $RMS_{\Lambda_{ci}}$ showing the difference between considering Λ_{ci} as an unique signal and separating it into positive and a negative components

4.5.1 Vortex Statistics

From Fig. 4.15b one is tempted to attempt a computation of basic vortex statistics. For example, one could treat "bluish" and "reddish" as separate plane bodies, with their densities and volumes equivalent to the color scales, i.e. Λ_{ci}, and areas, respectively. Thus each vortex would have its own "mass", that is a total swirling strength, and a "center of mass". These centroid positions can be calculated with traditional methods, so a study of number, size, and swirling strength of vortices is possible. One could represent those values as function of space, time or both, for instance. Because the turbulent flow is steady and fully developed, these options reduce

to the wall-normal y-position. For example, let us take an upper portion of Fig. 4.15b, mark an estimate position for the centroids of vortices, and count them by zones (see Fig. 4.17).

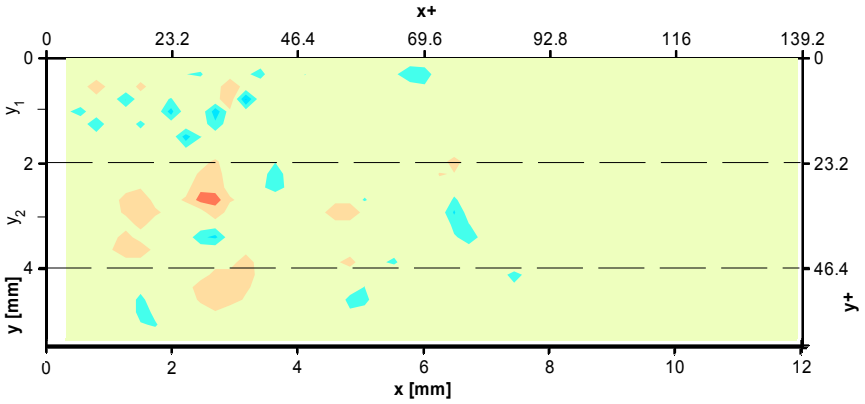

y	Positive Vortices	Negative Vortices
y_1	4	11
y_2	6	5

Fig. 4.17. Counting vortices from Fig. 4.15b

A program for doing PTV analysis that identifies, characterizes, and counts particles on a black background (Perez Estrada 2004) was modified and adapted to identify vortices along the 100 frames per data set. Then another software was utilized to perform the abovementioned basic statistics on those results, and finally a time average of all frame statistics was carried out. Fig. 4.18 shows the time averaged numbers of positive and negative vortices are plotted versus wall-normal position in inner units. In general, the presence of microbubbles is associated with an increase in the number of both positive and negative vortices up to $y+ \approx 100$.

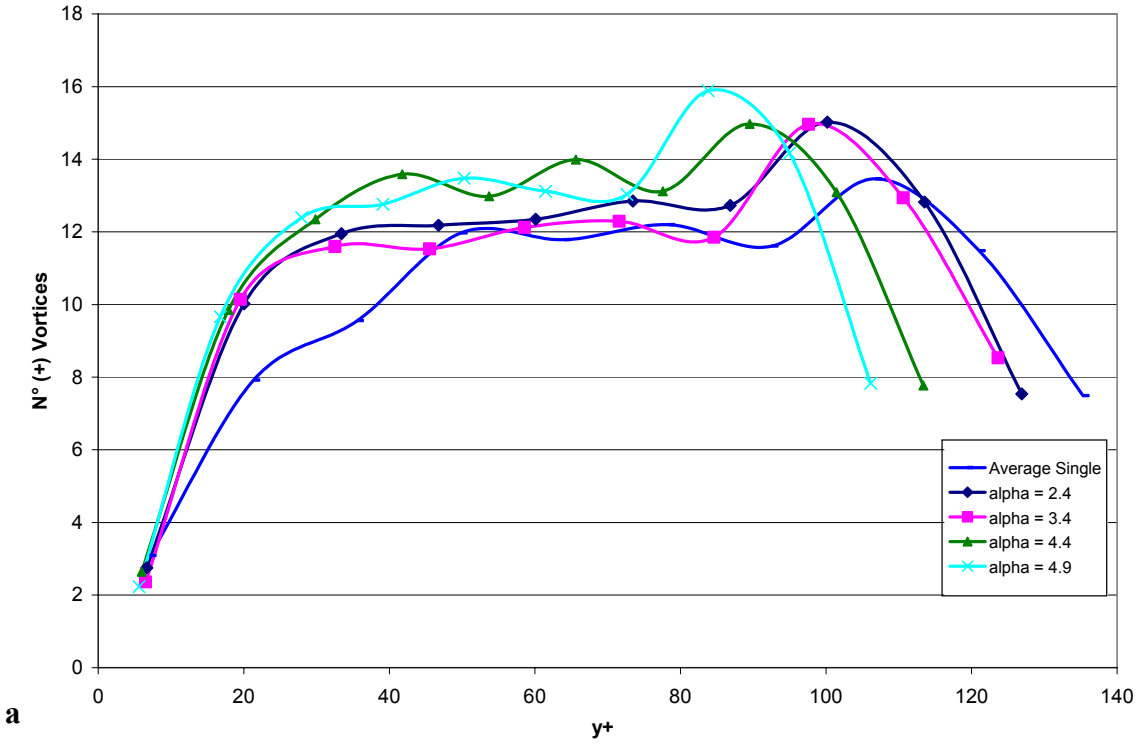

a

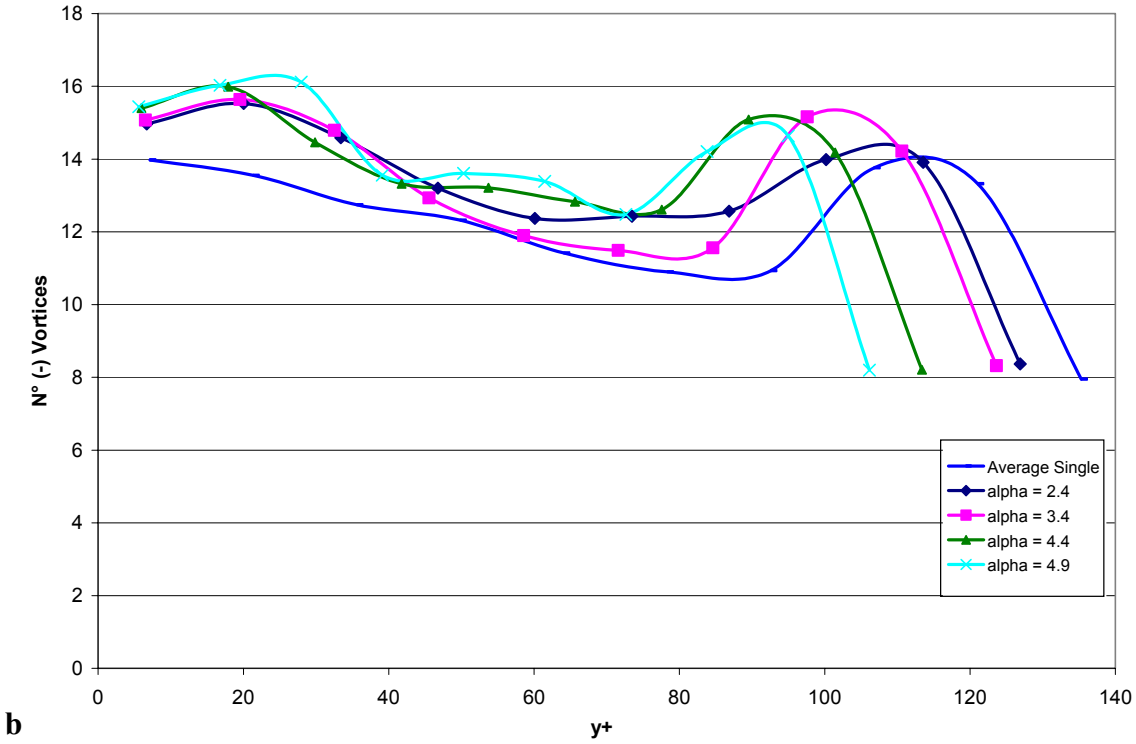

b

Fig. 4.18. Time averaged number of **a** positive; **b** negative vortices

In Fig. 4.19 and Fig. 4.20, the time averaged area (equivalent to the size) per positive and negative vortex, respectively, is plotted versus wall-normal position in inner units. It can be seen that, in general, the presence of microbubbles is associated with an decrease in the size of both positive and negative vortices.

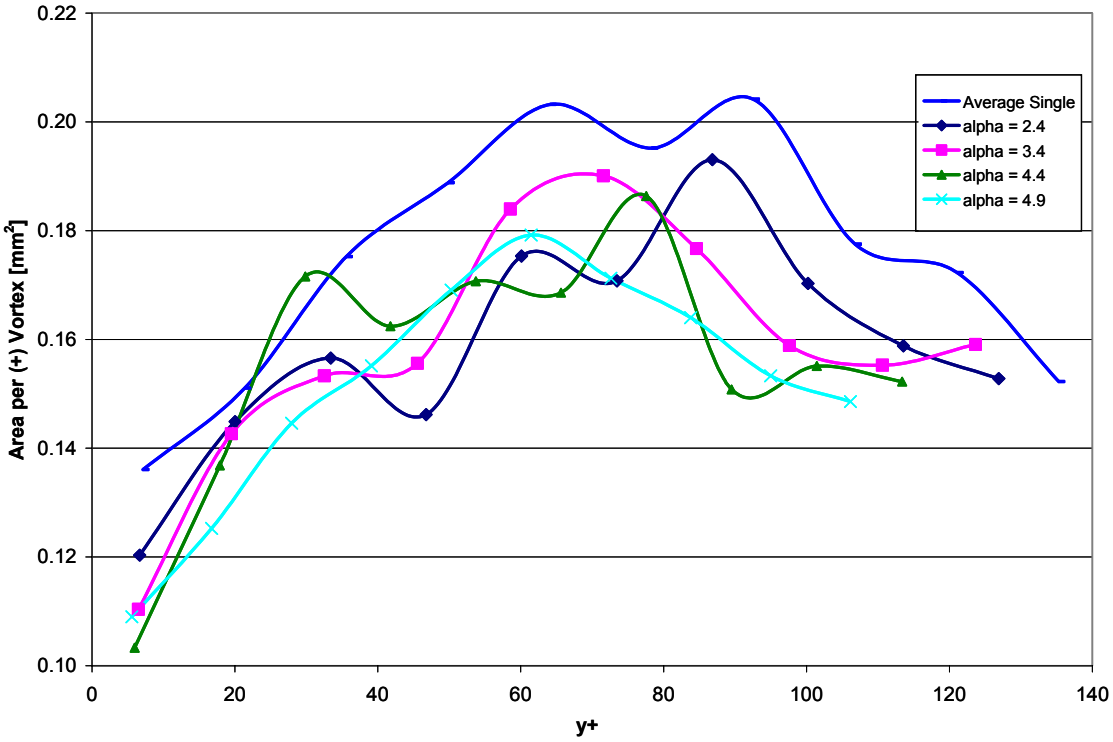

Fig. 4.19. Time averaged area per positive vortex

In Fig. 4.21, the time averaged swirling strength per positive and negative vortex, respectively, is plotted versus wall-normal position in inner units. The figure shows a general increase, when microbubbles are injected, in the swirling strength of positive vortices up to y+ ≈ 102, and negative vortices up to y+ ≈ 120.

Recalling from section 1 that the swirling strength gives the frequency of rotation

of the vortex about its axis, then figures 4.19 through 4.21 agree with the fact that smaller eddies will rotate at higher frequencies. However, it must be noted that, despite being smaller, vortices in two-phase are more numerous, as shown in Fig. 4.18.

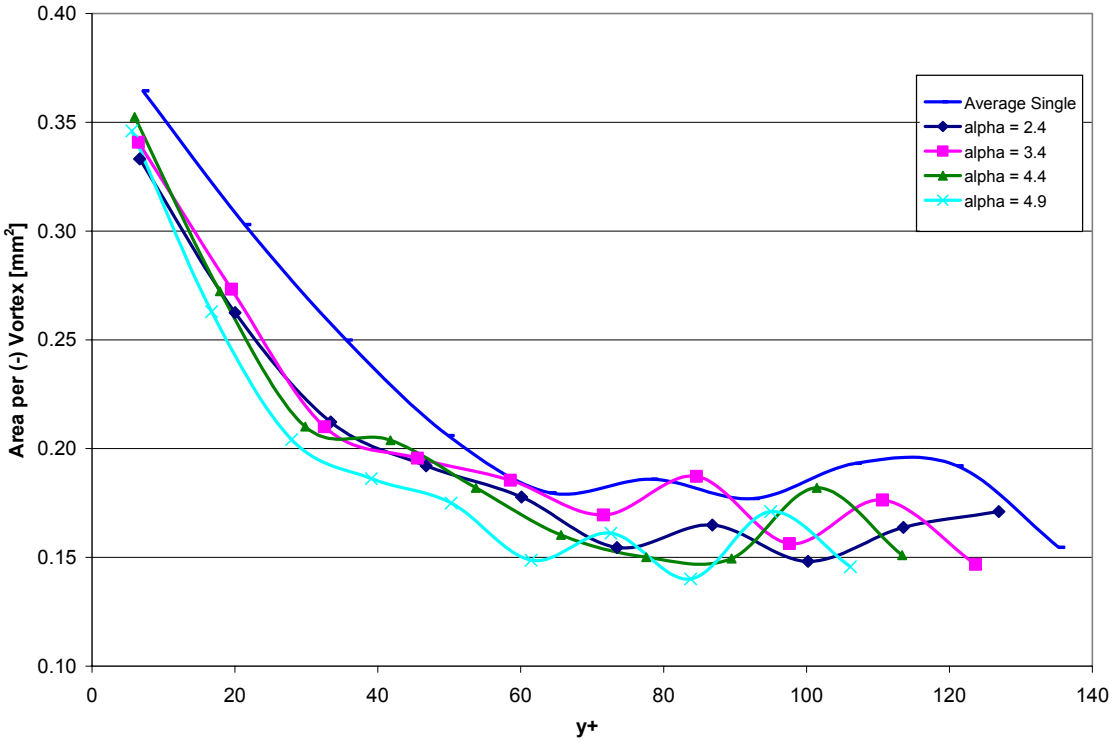

Fig. 4.20. Time averaged area per negative vortex

4.6 λ_2 Criterion

The λ_2 criterion, derived from the Hessian of pressure without the terms representing unsteady straining and viscous effects, is basically an improved local pressure minima criterion for vortex identification (Jeong and Hussain 1995). Although successfully applied so far (Jeong et al. 1997; Özsoy et al. 2005; among others), it is not direct the relationship of its magnitude to any vortex property, like in the λ_{ci} criterion.

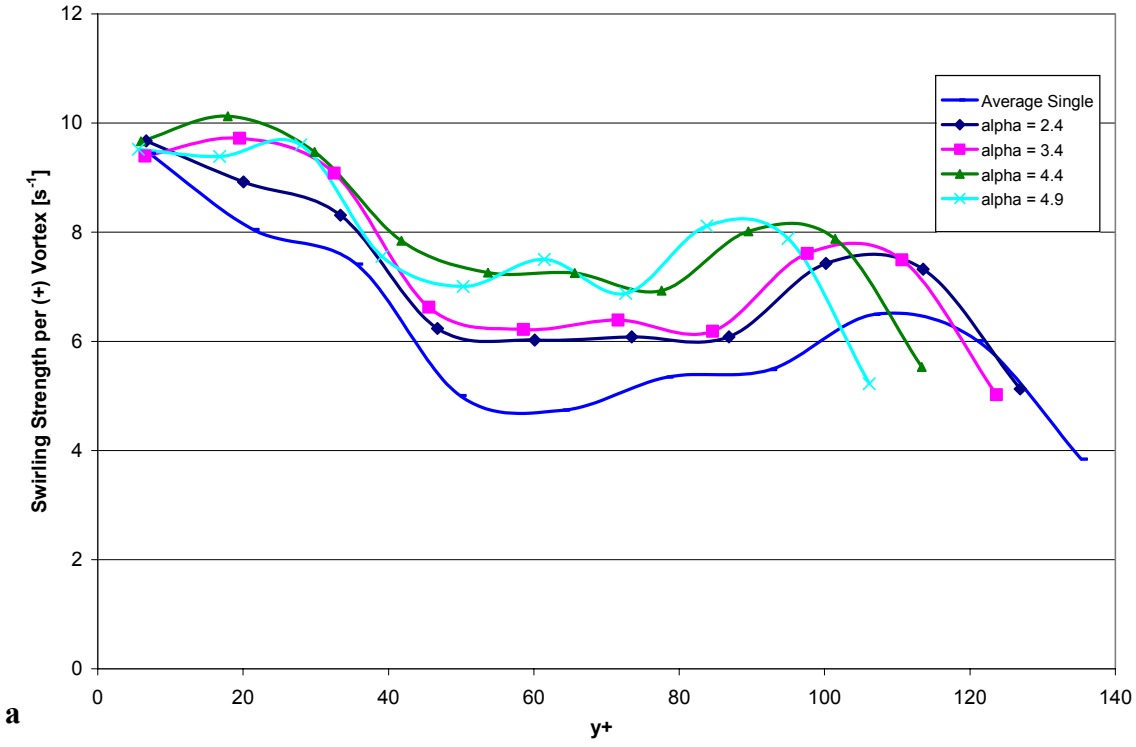

a

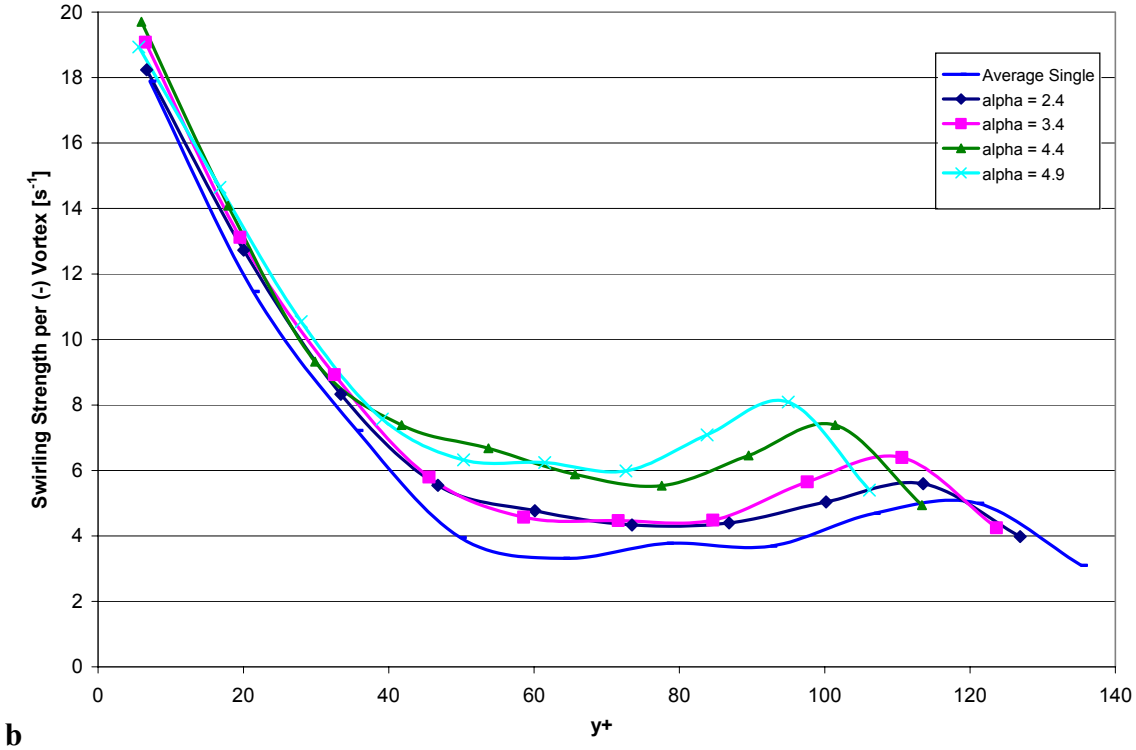

b

Fig. 4.21. Time averaged swirling strength per **a** positive; **b** negative vortex

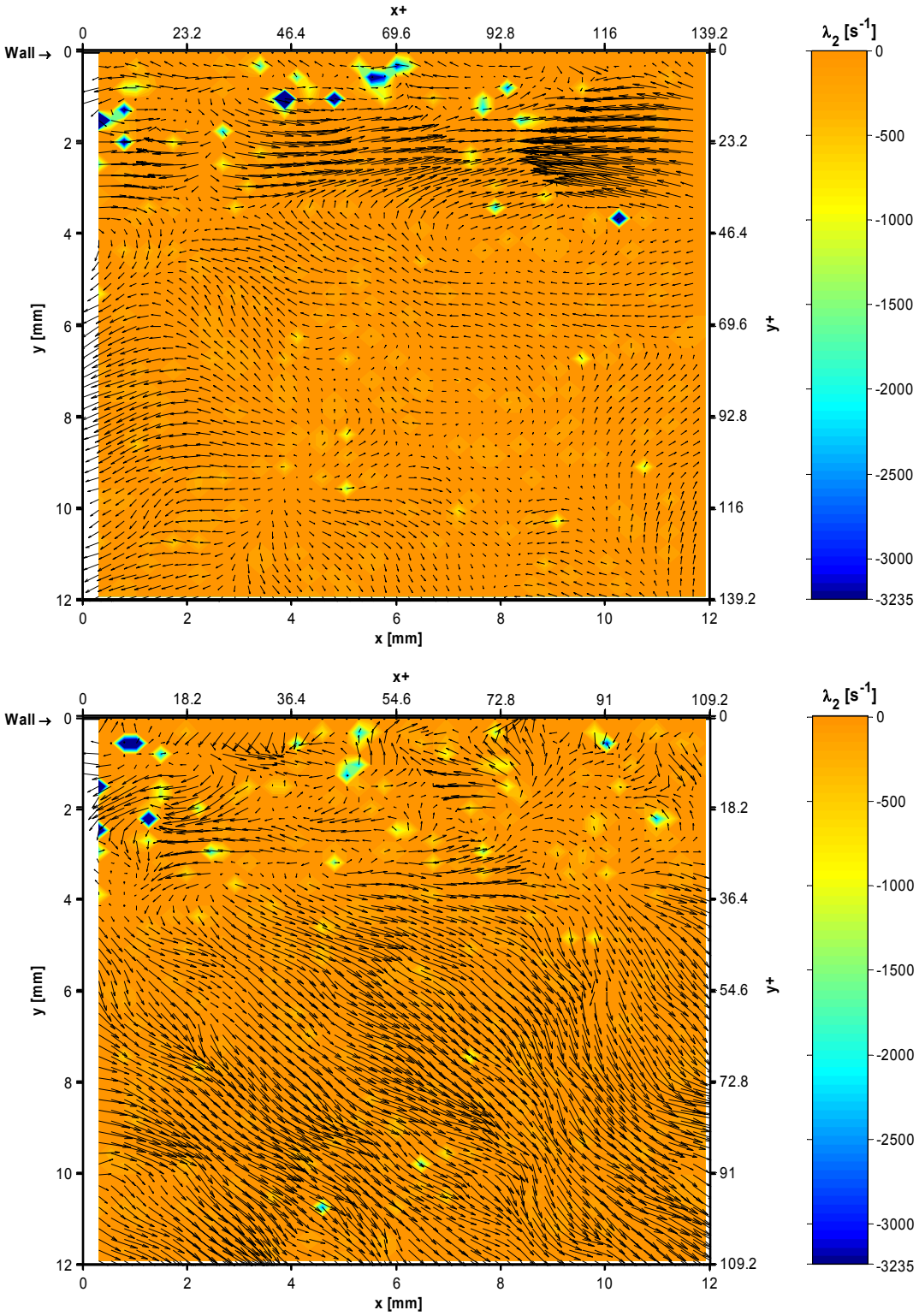

Fig. 4.22. Instantaneous λ_2 and Reynolds decomposed velocity field **a** Single phase, $f = 0.98$; **b** $\alpha = 4.9\%, f = 0.82$

A 2D version of the λ_2 criterion was derived by expressing the tensor $\mathbf{S}^2 + \mathbf{\Omega}^2$ was in 2-dimensional way:

$$\mathbf{S}^2 + \mathbf{\Omega}^2 = \begin{bmatrix} SO_{11} & SO_{12} \\ SO_{21} & SO_{22} \end{bmatrix} \tag{4.13}$$

Where:

$$SO_{11} = \left(\frac{\partial V_1}{\partial x_1}\right)^2 + \left(\frac{\partial V_1}{\partial x_2}\right)\left(\frac{\partial V_2}{\partial x_1}\right) \tag{4.14}$$

$$SO_{21} = SO_{12} = \frac{1}{2}\left(\frac{\partial V_1}{\partial x_1} + \frac{\partial V_2}{\partial x_2}\right)\left(\frac{\partial V_1}{\partial x_2} + \frac{\partial V_2}{\partial x_1}\right) \tag{4.15}$$

$$SO_{22} = \left(\frac{\partial V_2}{\partial x_2}\right)^2 + \left(\frac{\partial V_1}{\partial x_2}\right)\left(\frac{\partial V_2}{\partial x_1}\right) \tag{4.16}$$

The tensor $\mathbf{S}^2 + \mathbf{\Omega}^2$ given by equation 4.13 has two real eigenvalues because it is symmetric, thus a 2D version of the λ_2 criterion is to require that both eigenvalues, λ_1 and λ_2, be negative as a condition to have a vortex core. Therefore, if $\lambda_1 \leq \lambda_2$, it is enough that $\lambda_2 < 0$. This eigenvalue was calculated for single phase and $\alpha = 4.9$, and presented in Fig. 4.22 along with Reynolds decomposed flow fields. Compared to the λ_{ci} criterion, λ_2 proves more restrictive, producing much less background noise, and delineating less peaks, although with higher contrast and gradients.

5 SUMMARY

Different vortex identification and characterization methods have been applied to instantaneous two-dimensional velocity fields for both single and two-phase flows. The data was obtained from a measurement in a boundary layer of channel flows during the studies of the phenomenon of drag reduction by microbubble injection. In general, vorticity has shown total efficacy in marking zones of high shear stress. This would facilitate the study of drag reduction. However, it has proved of its incapability of identifying vortices in certain zones. The vorticity related to high shear may tend to mask that of the vortex cores. It was corrected with Galilean and Reynolds decompositions that can reveal those vortices whose cores convect at a certain velocity. Reynolds decomposition has been proved to be more suitable for revealing the vortices closer to the wall. However, these decompositions have an enormous drawback, which is that they require a priori information about t the convection velocity. That is what is called a frame-dependent scheme.

In contrast, frame-independent, or Galilean-invariant, vortex identification schemes do not change their outcomes if the flow field is measured from a frame moving at a constant velocity respect to its coordinate system. Some of those methods, based on critical point analysis and the invariants of the velocity and a modified pressure Hessian tensors, were applied and compared, achieving good results.

The λ_{ci} criterion, because of its direct relationship to the vortex nature (it is indeed inversely proportional to the period of rotation around the vortex axis) is well-

suited for the study of boundary layer drag reduction, even if it is not directly related to the shear stress as the vorticity.

In order to apply the λ_{ci} criterion to get vortex statistics in single and two-phase flows, it was modified by multiplying λ_{ci} with the vorticity sign. Consequently, positive and negative vortices could be discriminated. Vortex cores, which coincide with local λ_{ci} maxima, were isolated by filtering the λ_{ci} field with its root-mean-square RMS. It was found that, although both positive and negative vortices are smaller in two-phase than in single, they are present in more numbers. However, the swirling strength is higher in two-phase.

Another method for identifying vortices analyzed in this work is the λ_2 criterion. In general, it proved to be more restrictive and less prone to noise than the λ_{ci} criterion. It also presents vortex cores with isolated λ_2 peaks that have better contrast with the background. A drawback of this method is that, unlike the λ_{ci} criterion, it is not directly related to any vortex characteristic, like the period of rotation.

REFERENCES

Adrian RJ (1986) Multi-point optical measurements of simultaneous vectors in unsteady flow – a review. Int J Heat and Fluid Flow 7(2):127-145

Adrian RJ, Christensen KT, Liu ZC (2000) Analysis and interpretation of instantaneous turbulent velocity fields. Experiments in Fluids 29:275-290

Antonia RA, Browne LWB, Bisset DK (1988) Effect of Reynolds number on the organized motion in a turbulent boundary layer. In: Kline SJ, Afgan NH (eds) Near wall turbulence, Proceedings of Zoran Zaric Memorial Conference. Hemisphere, New York, pp 488-506

Barenblatt GI, Chorin AJ, Prostokishin VM (1997) Scaling laws for fully developed turbulent flow in pipes. Appl Mech Rev 50:413-429

Bernard PS, Wallace JM (2002) Turbulent flow. Analysis, measurement and prediction. John Wiley & Sons, Inc., Hoboken, New Jersey

Bradshaw P, Cebeci T, Fernholz HH, Johnston JP, Launder BE, Lumley JL, Reynolds WC, Woods JD (1976) Turbulence. Springer-Verlag, Berlin

Brooke JW, Hanratty TJ (1993) Origin of turbulence-producing eddies in a channel flow. Phys Fluids A 5(4):1011-1022

Chong MS, Perry AE, Cantwell BJ (1990) A general classification of three-dimensional flow fields. Phys Fluids A 2(5):765-777

Christensen KT, Wu Y (2004) A population study of small-scale spanwise vortices in turbulent channel flow. In: Proceedings of the 11th International Symposium on Flow Visualization, University of Notre Dame, Notre Dame, Indiana, 2004, pp 1-13

Christensen KT, Wu Y, Adrian RJ, Lai W (2004) Statistical imprints of structure in wall turbulence. AIAA 2004-1116

Chung TJ (2002) Computational fluid dynamics. Cambridge University Press, Cambridge, UK

Corrsin S, Kistler AL (1954) The free stream boundaries of turbulent flows. NACA TN 3133

Dominguez Ontiveros EE (2004) Wall pressure and PIV measurements and analysis for microbubble drag reduction investigation. MS thesis, Department of Mechanical Engineering, Texas A&M University, College Station, Texas

Durst F, Kikura H, Lekakis I, Jovanovic J, Ye Q (1996) Wall shear stress determination from near-wall mean velocity data in turbulent pipe channel flows. Experiments in Fluids 20:417-428

Gutierrez Torres CC (2004) Modification of turbulent structure in channel flows by microbubble injection close to the wall. PhD thesis, Department of Mechanical Engineering, Texas A&M University, College Station, Texas

Haller G (2005) An objective definition of a vortex. J Fluid Mech 525:1-26

Hanratty TJ (1956) Turbulent exchange of mass and momentum with a boundary. J Amer Institute Chemical Engrg. 2:3, 359

Hanratty TJ, Papavassiliou DV (1997) The role of wall vortices in producing turbulence. In: Panton RL (ed) Self-sustaining mechanisms of wall turbulence. Computational Mechanics Publications, Southampton, England, pp 83-108

Hassan YA, Blanchat TK, Seeley CH (1992) PIV flow visualization using particle tracking techniques. Meas. Sci. Technol. 3:633-642

Hassan YA, Gutierrez-Torres CC, Jimenez-Bernal JA (2004) Visualization of vortex structure in a channel flow by means of PIV with microbubble injection. In: Proceedings of the 11th International Symposium on Flow Visualization, University of Notre Dame, Notre Dame, Indiana, 2004

Hill MJM (1894) On a spherical vortex. Philosophical Transactions of the Royal Society London Ser A, 185, p 213

Hinze JO (1959) Turbulence. McGraw-Hill, New York

Hunt JCR, Wray AA, Moin P (1988) Eddies, stream, and convergence zones in turbulent flows. Center for Turbulence Research Report CTR-S88, pp 193-194

Jeong J, Hussain F (1995) On the identification of a vortex. J Fluid Mech 285:69-94

Jeong J, Hussain F, Schoppa W, Kim J (1997) Coherent structures near the wall in a turbulent channel flow. J Fluid Mech 332:185-214

Jiménez J, Moin P, Moser R, Keefe L (1988) Ejection mechanisms in the sublayer of a turbulent channel. Phys Fluids 31(6):1311-1313

Kim J (2003) Control of turbulent boundary layers. Phys Fluids 15(5):1093-1105

Kim J, Moin P (1986) The structure of the vorticity field in turbulent channel flow. Part 2. Study of ensemble-averaged fields. J Fluid Mech 162:339-363

Klebanoff PS (1954) Characteristics of turbulence in a boundary layer with zero pressure gradient. NACA TN 3178

Klewicki JC (1997) Self-sustaining traits of near-wall motions underlying boundary layer stress transport. In: Panton RL (ed) Self-sustaining mechanisms of wall turbulence. Computational Mechanics Publications, Southampton, England, pp 135-166

Kline SJ, Robinson SK (1988) Quasi-coherent structures in the turbulent boundary layer. Part I - Status report on a community-wide summary of the data. In: Kline SJ, Afgan NH (eds) Near wall turbulence, Proceedings of Zoran Zaric Memorial Conference. Hemisphere, New York, pp 200-217

Lamb H (1932) Hydrodynamics. Cambridge University Press, Cambridge, UK

Laufer J (1953) The structure of turbulence in a fully developed pipe flow. NACA TN 2954

Liu Z, Adrian RJ, Hanratty TJ (2001) Large-scale modes of turbulent channel flow: transport and structure. J Fluid Mech 448:53-80

Lugt HJ (1979) The dilemma of defining a vortex. In: Müller U, Roesner KG, Schmidt B (eds) Recent developments in theoretical and experimental fluid mechanics. Springer-Verlag, Berlin, pp 309-321

Moin P, Leonard A, Kim J (1986) Evolution of a curved vortex filament into a vortex ring. Phys Fluids 29(4):955-963

Özsoy E, Rambaud P, Stitou A, Riethmuller ML (2005) Vortex characteristics in laminar cavity flow at very low Mach number. Experiments in Fluids 38:133-145

Panton RL (1984) Incompressible flow. John Wiley and Sons, New York

Perez Estrada CE (2004) Analysis, comparison and modification of various particle image velocimetry (piv) algorithms. MS thesis, Department of Nuclear Engineering, Texas A&M University, College Station, Texas

Raffel M, Willert C, Kompenhans J (1998) Particle image velocimetry: a practical guide. Springer-Verlag, Berlin

Reynolds O (1895) On the dynamical theory of incompressible viscous fluids and the determination of the criterion. Philos Trans R Soc London Ser A, 186:185-213

Robinson SK, Kline SJ, Spalart PR (1988) Quasi-coherent structures in the turbulent boundary layer. Part II – Verification and new information from a numerically simulated flat-plate layer. In: Kline SJ, Afgan NH (eds) Near wall turbulence, Proceedings of Zoran Zaric Memorial Conference. Hemisphere, New York, pp 218-247

Rubin H, Atkinson J (2001) Environmental fluid mechanics. Marcel Dekker, New York

Runstadler PW, Kline SJ, Reynolds WC (1963) An experimental investigation of the flow structures of the turbulent boundary layer. Report MD-8, Thermosciences Division, Dept Mech Eng, Stanford University, 1963

Schlichthing H, Gersten K (2000) Boundary layer theory. Springer-Verlag, Berlin

Schoppa W, Hussain F (1998) A large-scale control strategy for drag reduction in turbulent boundary layers. Phys Fluids 10(5):1049-1051

Schoppa W, Hussain F (2002) Coherent structure generation in near-wall turbulence. J Fluid Mech 453:57-108

Tatsumi T (1984) Irregularity, regularity and singularity of turbulence. In: Tatsumi T (ed) Proceedings of the international symposium on turbulence and chaotic phenomena in fluids, Kyoto, Japan, September 1983, pp 1-4

Taylor GI (1923) Stability of a viscous liquid contained between two rotating cylinders. Philosophical Transactions of the Royal Society London Ser A, 223:289-343

Taylor GI (1935) Statistical theory of turbulence. In: Proceedings of the Royal Society London Ser A, 151:421-444

Theodorsen T (1952) Mechanism of turbulence. In: Proceedings of the 2nd Midwestern Conference on Fluid Mechanics, Ohio State University, Columbus, Ohio, 1952, pp 1-19

Townsend AA (1956) The structure of turbulent shear flow. Cambridge University Press, 2nd edition, Cambridge, UK

Tsinober A (2001) An informal introduction to turbulence. Kluwer Academic Publishers, Dordrecht, The Netherlands

Uemura T, Yamomoto F (1993) A high speed algorithm for 2D and 3D and its application. In: Proceedings of the 6th International Symposium on Transport Phenomena in Thermal Engineering, Seoul, Korea, 1993, pp 323-332

van de Hulst HC (1981) Light scattering by small particles. Dover Publications, New York

Wallace JM, Eckelmann H, Brodkey RS (1972) The wall region in a turbulent shear flow. J Fluid Mech 54:39-48

Willmarth WW, Lu SS (1972) Structure of the Reynolds stress near the wall. J Fluid Mech 55:65-92

Wu Y (2004) Spatial characteristics of outer-layer vortex organization in turbulent channel flow. MS thesis, Department of Mechanical Engineering, The University of New Mexico, Albuquerque, New Mexico

Zhou J, Adrian RJ, Balanchandar S (1996) Autogeneration of near-wall vertical structures in channel flow. Phys Fluids 8:288-290

Zhou J, Adrian RJ, Balanchandar S, Kendall TM (1999) Mechanisms for generating coherent packets of hairpin vortices in channel flow. J Fluid Mech. 387:353-396

VITA

Adrian Gaston Maroni Veiga was born in Embarcacion, Argentina, on March 30, 1977. In 2001 he graduated from the Instituto Universitario Aeronautico with a Bachelor of Science in mechanical and aeronautical engineering.

In September 2003 he joined the Master of Science program in mechanical engineering at Texas A&M University. During the summer 2004 he started his studies under Dr. Yassin A. Hassan's tutelage.

Contact Information: Nuclear Engineering Department

Texas A&M University

College Station, TX. 77843-3133

(Dr. Yassin A. Hassan)

gmaroni@gmail.com